

Linking discrete and continuous models of cell birth and migration

W. Duncan Martinson¹, Alexandria Volkening², Markus Schmidtchen³, Chandrasekhar Venkataraman⁴, and José A. Carrillo¹

¹Mathematical Institute, University of Oxford, Oxford, UK

²Department of Mathematics, Purdue University, West Lafayette, Indiana, USA

³Institute of Scientific Computing, Technische Universität Dresden, Dresden, Germany

⁴Department of Mathematics, University of Sussex, Brighton, UK

April 5, 2024

Abstract

Self-organisation of individuals within large collectives occurs throughout biology. Mathematical models can help elucidate the individual-level mechanisms behind these dynamics, but analytical tractability often comes at the cost of biological intuition. Discrete models provide straightforward interpretations by tracking each individual yet can be computationally expensive. Alternatively, continuous models supply a large-scale perspective by representing the “effective” dynamics of infinite agents, but their results are often difficult to translate into experimentally relevant insights. We address this challenge by quantitatively linking spatio-temporal dynamics of continuous models and individual-based data in settings with biologically realistic, time-varying cell numbers. Specifically, we introduce and fit scaling parameters in continuous models to account for discrepancies that can arise from low cell numbers and localised interactions. We illustrate our approach on an example motivated by zebrafish-skin pattern formation, in which we create a continuous framework describing the movement and proliferation of a single cell population by upscaling rules from a discrete model. Our resulting continuous models accurately depict ensemble average agent-based solutions when migration or proliferation act alone. Interestingly, the same parameters are not optimal when both processes act simultaneously, highlighting a rich difference in how combining migration and proliferation affects discrete and continuous dynamics.

Key Words: non-local interactions; zebrafish; self-organisation; aggregation equations

1 Introduction

Self-organisation of individual agents is a key feature of life. It occurs ubiquitously throughout the natural world, from the macroscopic example of bird flocking [1–4] to the microscopic phenomenon of cell sorting during development [5–9]. The degree to which members of a group coordinate their movement, proliferation, and competition accounts for pattern diversity across biological scales. Alongside experimental approaches, mathematical models can help identify the underlying behaviours that give rise to specific collective dynamics. However, a trade-off often exists between tractability and detail when building models of pattern formation, due in part to the multiscale nature of biological systems. Consequently, better quantitative characterisation of the relationship between analytically tractable models and more biologically representative approaches will improve our understanding of self-organisation throughout nature.

Here, we help address this open challenge using pigment cell dynamics in zebrafish patterns as a motivation. The zebrafish (*Danio rerio*) is a popular model organism for studying pattern formation, as dark stripes and gold interstripes emerge in its skin during development [10–13]. As we show in Fig. 1, these stripes result from

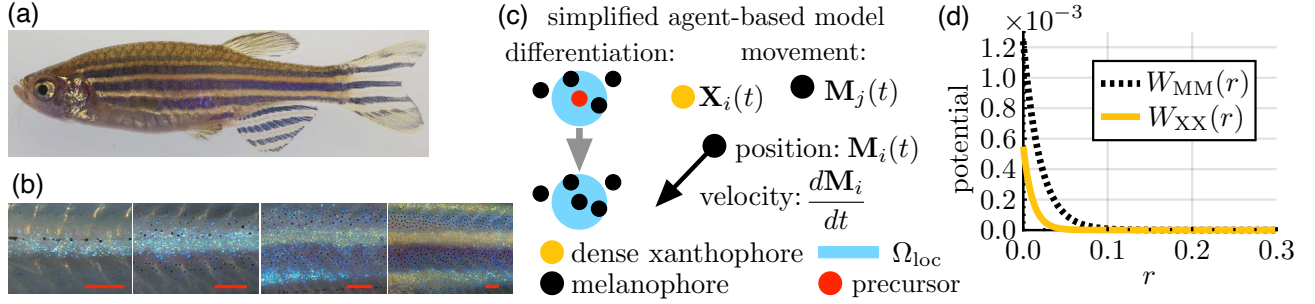


Figure 1: Motivating biological example and model. (a) Wild-type zebrafish feature stripe patterns in their skin. These patterns consist of several types of brightly coloured pigment cells. (b) Over the course of a few months, these cells organise sequentially into stripes and interstripes from the centre of the fish body outward [10]. (c) For the purposes of this manuscript, we focus on a single population of black melanophores or gold dense xanthophores, using a simplified version of the model from [21]. The agent-based model (ABM) [21] that motivates our work describes how patterns arise through cell differentiation, competition, and movement. In our simplified version of the ABM [21], we assume new cells appear at randomly selected locations based on short-range activation; this models cell differentiation from uniformly distributed precursors (red position) [21], and we also refer to this as “proliferation” or “birth” in this paper. (We describe the cell-differentiation rules in the full model [21] in more detail in Supplementary Fig. 1.) In both our work and the ABM [21], cell movement is deterministic and governed by ordinary differential equations (ODEs). (d) These ODEs account for cell–cell repulsion through potential functions, which describe melanophore–melanophore (W_{MM}) and xanthophore–xanthophore (W_{XX}) interactions as a function of their pairwise distance r . Red scale bar is 250 micrometres (μm) in (b). Image (a) adapted from Fadeev *et al.* [22] and licensed under CC-BY 4.0 (<https://creativecommons.org/licenses/by/4.0/>). Image (b) adapted from Frohnhofer *et al.* [10] and licensed under CC-BY 3.0 (<https://creativecommons.org/licenses/by/3.0/>); published by The Company of Biologists Ltd.

the coordination of interactions among several types of cells, including black melanophores and gold (dense) xanthophores [10, 14–18]. Experiments that perturb stripes—i.e., by laser ablation [14, 19]—demonstrate how cell–cell signalling and external cues contribute to the creation of alternative motifs such as spots or labyrinths. A rich diversity of mutant patterns, including widened or curvy stripes, also emerge when cell interactions are altered due to genetic mutations [17, 20].

Data-driven mathematical models can help uncover the drivers of zebrafish pattern formation and other biological phenomena exhibiting self-organisation by identifying important phase transitions, isolating the effects of specific processes such as cell division, and providing hypotheses that can guide the design of *in vivo* experiments [23–26]. Different modelling frameworks yield insight at the population or individual level, depending on how they represent members of a group. One modelling approach involves tracking how the position of each individual changes in time. These so-called “discrete” systems include centre-based models [27, 28], cellular automata [29, 30], cellular Potts models [31, 32], and vertex models [33, 34]. Within the setting of zebrafish patterning, agent-based models (ABMs) have been developed that restrict cells to occupy certain locations “on-lattice” [35–37] or allow them to roam freely, “off-lattice”, in the domain [21, 38–40]. Due to their ability to work on the same length scales as empirical data, ABMs provide an intuitive connection to experiments and allow for detailed predictions about how interactions between agents drive group behaviours. However, ABMs can be prohibitive to simulate when the number of individuals is large, and understanding their long-time behaviour under alternative rules and parameters relies on extensive computation [41].

A second modelling approach uses continuous functions to represent the “average” density of agents in a collective, with their dynamics governed by a partial differential equation (PDE) in space and time. Continuous models, including reaction-diffusion equations, Boltzmann-like kinetic equations, and integro-differential

equations (IDEs), typically cannot resolve individuals and, instead, track the ensemble average (EA) behaviour of a population. However, these models are more amenable to mathematical analysis and more readily provide insight into long-term behaviour than discrete frameworks do [42, 43]. For example, changes in patterning may arise because of Turing-like instabilities [44–46] or due to alterations in physically-based interactions such as cell–cell adhesion [7, 38, 47–50]. In the case of zebrafish patterns, researchers have applied a wide swath of continuous models—including reaction-diffusion equations [14, 19, 35, 51, 52] and non-local PDEs [7, 53–55]—to better understand cell dynamics.

Despite the differences between discrete and continuous approaches, it is possible to establish a mathematical link between these representations in the limit of infinite individuals. This procedure, known as “coarse-graining”, derives differential equations from a given discrete model and yields information about its EA behaviour [56–62]. For example, the authors in [63–65] derive logistic IDEs from stochastic processes that describe the birth and death of individuals undergoing Darwinian evolution in the limit of large numbers. Coarse-grained descriptions become inaccurate when relatively few individuals are present, however, as is the case in many biological contexts such as pattern formation in zebrafish. Many approaches also neglect potentially important spatial correlations between cells—caused, for instance, by division or competition—that may play a critical role in pattern dynamics [52, 66–71]. While it is possible to go beyond this “mean-field” setting by deriving continuous models that respect higher-order correlations [72–76] and hard-core interactions [77], these methods still rely on simplifying assumptions that introduce errors between the discrete and continuous frameworks. Controlling these errors in a biological setting is an important objective.

We help tackle this problem by developing a pipeline to minimise spatio-temporal discrepancies between continuous models and individual-based data in settings with biologically relevant, dynamic cell numbers. The method relies on fitting parameters that effectively dilate the time variable of continuous-model solutions. Our approach can be used to describe biological self-organisation in systems whose macroscopic description can be derived or inferred. We apply our approach to a case study motivated by stripe formation in zebrafish skin, as this allows us to illustrate its utility and interpretability for experimentally measurable quantities with biologically meaningful spatial and temporal units. In §2, we describe the ABM that we simulate to generate synthetic individual-based data associated with self-organising phenomena. In its full form, the ABM motivating our work [21] admits pattern formation via non-local rules for cell birth, death, and movement that are inspired by the underlying biology of zebrafish-skin patterns (Fig. 1) [21, 40]. To focus on the presentation of our pipeline, however, we simplify some biological complexity by reducing this model [21] to focus on a single cell type—melanophores or dense xanthophores, respectively. (We plan to extend this pipeline to multiple cell types in future work.) We then detail the corresponding continuous descriptions and our method for matching their solutions to EA ABM data even in scenarios with finite and time-dynamic cell numbers. We present our results for black melanophores in §3, and—as a means of demonstrating the generality of our methodology—apply the same approach to dense xanthophores in the Supplementary Information (SI)-§6.

2 Mathematical models and methods

In §2.1, we develop our ABM for cell migration and derive its continuous counterpart. Subsequently, in §2.2, we introduce our discrete model for cell birth and develop a corresponding continuous IDE model. We present our full models of migration and proliferation in §2.3. Lastly, we present our approach to estimating scaling parameters in our continuous models from EA ABM data in §2.4. Following previous ABMs [21, 40] of pattern formation in zebrafish, we assume (1) migration is governed by conservative forces between pigment cells and (2) non-local interactions inform cell birth in a two-dimensional (2D) plane [21, 39, 40]. Throughout this paper,

we refer to:

$$\begin{aligned}\Omega \subset \mathbb{R}^2 &= \text{domain of the simulation with spatial units of millimetres (mm),} \\ \mathbb{R}^2 \ni \mathbf{M}_i(t) &= \text{coordinates of the centre of the } i^{\text{th}} \text{ melanophore at } t \text{ days in our discrete models,} \\ \mathbb{N} \ni N_M(t) &= \text{total number of melanophores present at time } t \text{ days, and} \\ \mathbb{R}_{\geq 0} \ni M(\mathbf{x}, t) &= \text{density of melanophores at position } \mathbf{x} \text{ and time } t \text{ in cells/mm}^2,\end{aligned}$$

with the exception of Fig. 7 where we consider a one-dimensional (1D) domain; there $M(\mathbf{x}, t)$ is the number density of melanophores in cells/mm. Because it appears several times, we define the indicator function $\mathbb{1}_{\{\text{condition}\}}$ here, as:

$$\mathbb{1}_{\{\text{condition}\}}(x) = \begin{cases} 1, & \text{if } x \text{ satisfies the rule specified by “condition”,} \\ 0, & \text{otherwise,} \end{cases} \quad (1)$$

where “condition” depends on the model rule and cell interaction, as we discuss next.

2.1 Models of migration

Our ABM for cell movement tracks the position, $\mathbf{M}_i(t)$, of each cell, indexed by $i \in \{1, \dots, N_M(t)\}$, at time $t \geq 0$. The movement of each melanophore depends on its interactions with surrounding melanophores, following an overdamped version of Newton’s second law. The forces are assumed to be conservative, i.e., they may be written as the gradient of a potential. This leads to the following system:

$$\frac{d\mathbf{M}_i}{dt} \approx \mathbf{F}_{\text{int}}^{(i)} = - \sum_{j=1, j \neq i}^{N_M(t)} \nabla W_{MM}^c(\mathbf{M}_i - \mathbf{M}_j). \quad (2)$$

Here, $\mathbf{F}_{\text{int}}^{(i)}$ is the net force arising from all cell–cell interactions according to the potential $W_{MM}(\mathbf{r})$, where \mathbf{r} is the inter-particle displacement. The potential can encode cell–cell repulsion and adhesion, depending on the sign of its gradient along the direction between two cell centres. Many choices for $W_{MM}(\mathbf{r})$ are possible, including harmonic, power-law, Morse, and Leonard-Jones potentials, among others. Here we use exponential potentials given by:

$$W_{MM}(\mathbf{r}) = R_{MM}e^{-|\mathbf{r}|/\omega_{MM}} - A_{MM}e^{-|\mathbf{r}|/a_{MM}}, \quad (3)$$

in accordance with prior ABMs of pattern formation in zebrafish [21, 40]; see Fig. 1(c) and Table 1 for parameter values and their biological interpretations. To model cells communicating through cellular extensions or dendrites [17, 18], secreted signals [78], or cell–cell contact [79], we assume forces on cells are zero beyond some cut-off distance d_{max} . We represent this using the notation $\nabla W_{MM}^c(\mathbf{r}) = \nabla W_{MM}(\mathbf{r}) \mathbb{1}_{\{|\mathbf{r}| < d_{\text{max}}\}}(\mathbf{r})$, and set $N_M(t) = N_M$ when there is no cell birth. We remark that the model given by Eqn. (2) is deterministic in the sense that it does not include Brownian motion.

The associated continuous model describes the melanophore density, $M(\mathbf{x}, t)$. Integrating $M(\mathbf{x}, t)$ over a bounded region yields the total number of melanophores within that area at time t . Following the coarse-graining procedure in [60, 80, 81], an outline of which is found in the SI-§1.1, we obtain the PDE below:

$$\frac{\partial M}{\partial t} = \alpha_{MM} \nabla \cdot (M \nabla W_{MM}^c \star M), \quad (4)$$

where the force ∇W_{MM}^c is the same as in Eqn. (2) and \star is the convolution operator [21, 40]. The parameter α_{MM} in Eqn. (4) is not inherent to the coarse-graining procedure; rather, it accounts for possible differences between the discrete and continuous models. Indeed, simulating Eqn. (4) with the parameter values listed in

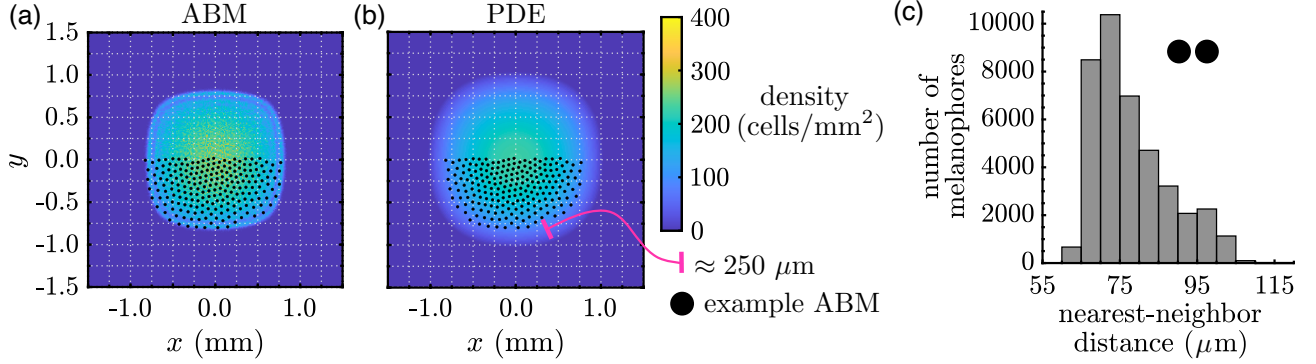


Figure 2: The PDE for cell migration does not accurately describe the EA ABM result when its scaling parameter α_{MM} is set to unity. (a) To compute our EA ABM result, we solve Eqn. (2) using an initial condition of 400 melanophores placed uniformly at random in a 1 mm \times 1 mm square, group cell positions in a 240×240 histogram, and average such data over 10^4 ABM realisations. (b) We compute the corresponding PDE solution by simulating Eqn. (4) with $\alpha_{\text{MM}} = 1$ from a uniform density of 400 cells/mm² in the same square region. The ABM and PDE solutions use the same potential (given by Eqn. (3) with parameters in Table 1). We overlay an example ABM realisation for comparison; the results demonstrate that the support of the PDE is larger than that of the ABM by about 200 to 250 μm . Because melanophore–melanophore distances have been measured to be roughly 50 μm *in vivo* [82] and stripes are only about 7–12 cells wide [14], this is a large difference. (c) The distribution of nearest-neighbor distances across 100 ABM realisations demonstrates that cell–cell separation ranges from roughly 60 to 100 μm . Based on visual inspection of the graphs, nearest-neighbor distances appear inversely proportional to the EA cell density. In (a)–(c), we show results at $t = 150$ days.

Table 1 and $\alpha_{\text{MM}} = 1$ (the value expected from the mean-field approximation) does not always capture the ABM dynamics; see Fig. 2. The individual and EA ABM results demonstrate that cells disperse until they are about 55–115 μm apart at $t = 150$ days. The PDE with $\alpha_{\text{MM}} = 1$, however, predicts that cells travel about 250 μm further in the same time period. Additionally, the PDE cell density is lower than the EA ABM density near the centre of the domain, implying that cells are more separated there. The continuous solution at earlier times more closely resembles the EA ABM result at $t = 150$ days, however, which suggests that PDE solutions evolve at a faster time scale than that of the discrete model. The parameter α_{MM} effectively dilates the time variable, such that solutions travel α_{MM} times more quickly. Thus, a non-unitary value of α_{MM} is likely to produce a better match between the discrete and continuous solutions. To our knowledge, the value of α_{MM} cannot be derived *a priori*. Instead, we develop an approach for estimating its value based on ABM data in §2.4, and will pursue an analytic derivation for this parameter in future work.

2.2 Models of cell birth

Our ABM for cell birth consists of stochastic, discrete-time rules which we adapt and simplify from [21] (motivation for these rules may be found in the SI-§1.2). Specifically, at each time step (i.e., day) in a simulation we select $N_{\text{bir}} \in \mathbb{N}$ locations uniformly at random from Ω and evaluate them synchronously for possible cell birth. Each selected location, \mathbf{z} , represents the position of a precursor cell that may differentiate into a melanophore based on the signals that it receives. The conditions for melanophore birth in the ABM [21] depend on both neighboring melanophores and dense xanthophores, as we show in Supplementary Fig. 1. Since we restrict to one population in this manuscript, we simplify the rules from [21]; see SI-§1.2 for details. In particular, a new

melanophore emerges at position \mathbf{z} according to the rule:

$$\underbrace{\sum_{i=1}^{N_M} \mathbb{1}_{\{\mathbf{M}_i \in \Omega_{\text{loc}}^{\mathbf{z}}\}}(\mathbf{M}_i) \geq 1}_{\text{short-range activation}} \quad \text{and} \quad \underbrace{\sum_{i=1}^{N_M} \mathbb{1}_{\{\mathbf{M}_i \in \Omega_{\text{loc}}^{\mathbf{z}}\}}(\mathbf{M}_i) < c_{\text{ABM}}^+}_{\text{overcrowding prevention}} \quad \longrightarrow \quad \text{melanophore appears at } \mathbf{z}, \quad (5)$$

where $c_{\text{ABM}}^+ \in \mathbb{N}$, and

$$\Omega_{\text{loc}}^{\mathbf{z}} = \text{disk centred at } \mathbf{z} \text{ with radius } d_{\text{loc}}. \quad (6)$$

According to Eqn. (5), new cells appear near existing melanophores until the maximum number of cells—namely, c_{ABM}^+ —in $\Omega_{\text{loc}}^{\mathbf{z}}$, the interaction region between cells, is reached, see Table 1 for parameter values. While Eqn. (5) is deterministic, stochasticity enters our ABM through our N_{bir} randomly selected positions $\{\mathbf{z}\}$. Similar stochastic rules can also be used to model cell death, as in [21, 40], although we do not consider them here.

We do not know of existing methods for rigorously deriving continuous models of cell birth from off-lattice ABMs with this noise structure. We therefore adopt a phenomenological modelling approach, in which we create a phenomenological continuous model whose governing equations mimic the stochastic interaction rules. We reason that the number density of cells in a continuous model must increase at a constant rate (proportional to N_{bir}) when continuous versions of the overcrowding and short-range activation restrictions are met, since this occurs at the individual level in the ABM. Furthermore, we represent the density restrictions with an indicator function using the integral of the number density over Ω_{loc} as an argument, since the latter quantity yields the total number of cells within that region. This leads to the continuous model below:

$$\frac{\partial M}{\partial t}(\mathbf{x}, t) = \gamma N_{\text{bir}} \mathbb{1}_{\left\{1 \leq \int_{\Omega_{\text{loc}}^{\mathbf{x}}} M(\mathbf{y}, t) d\mathbf{y} < c^+\right\}}(\mathbf{x}, t), \quad (7)$$

where c^+ is the continuous equivalent of the density-limiting parameter c_{ABM}^+ in Eqn. (5); N_{bir} has the same value as in our corresponding; and $\gamma \in \mathbb{R}^+$ is a parameter that effectively dilates the time variable in a similar way as α_{MM} in the cell-movement model. The units of γ must be inversely proportional to those of the domain size in order to make the dimensions of Eqn. (7) consistent. Its value is unknown, however we can employ a phenomenological argument to determine an expected value by integrating Eqn. (7) over the whole domain. This yields an upper bound on the number of cells born per unit time of $\gamma N_{\text{bir}} |\Omega|$, hence one expects $\gamma \approx |\Omega|^{-1}$ to maintain a maximum rate of N_{bir} cells born per day as in our ABM. We note, however, that this argument does not take into account possible clustering or other spatial correlations that can occur in the ABM, which may change the values of γ and c^+ from their expected values. While we could address this by allowing both parameters to depend on the proportion of the domain in which the birth conditions are fulfilled, we leave this extension for a future study and simply estimate uniform values for γ and c^+ by fitting to EA ABM data, as we do for α_{MM} in the movement-only model. We overview our approach for estimating the values of c^+ and γ in §2.4.

2.3 Full models of cell movement and birth

We combine our descriptions of cell movement and proliferation to form our full discrete and continuous models. For our full ABM, we move cells according to Eqn. (2) and then introduce new agents based on Eqn. (5) at each simulated day; see the SI-§2 for details. For our continuous model, we combine the terms related to movement and birth, such that the cell density evolves according to:

$$\frac{\partial M}{\partial t}(\mathbf{x}, t) = \alpha_{\text{MM}} \nabla \cdot (M \nabla W_{\text{MM}}^c \star M) + \gamma N_{\text{bir}} \mathbb{1}_{\left\{1 \leq \int_{\Omega_{\text{loc}}^{\mathbf{x}}} M(\mathbf{y}, t) d\mathbf{y} < c^+\right\}}(\mathbf{x}, t), \quad (8)$$

Parameter	Value	Description and motivation
R_{MM}	0.00124 mm ² /day	Strength of melanophore repulsion potential in Eqn. (3); based on [21, 39]
A_{MM}	0 mm ² /day	Strength of melanophore adhesion potential in Eqn. (3); based on [21, 39]
ω_{MM}	0.02 mm	Melanophore repulsion interaction range in Eqn. (3); based on [21, 39]
a_{MM}	0.012 mm	Melanophore adhesion interaction range in Eqn. (3); based on [21, 39]
d_{max}	0.2 mm	Maximum cell interaction distance in Eqn. (2); based on [21, 39]
d_{loc}	0.075 mm	Maximum interaction range for cell birth in Eqn. (6); based on [21] and chosen slightly larger than measurements of cell–cell distances [82, 83]
N_{bir}	Varies	Number of positions selected uniformly at random per day for possible cell proliferation (e.g., differentiation from precursors) in Eqns. (5) and (7)
c^-	1 cell	Lower bound for the number of cells in a short-range neighborhood for cell proliferation in Eqns. (5) and (7)
c^+	6 cells	Upper bound for the number of cells in a short-range neighborhood for birth in Eqns. (5) and (7); based on estimations of data [14, 82] in [21]
t_{final}	150 or 2,000 days	Simulation end time (150 days in 2D and 2,000 days in 1D)
Δt_{move}	0.01 or 0.1 days	Time step for numerical implementation of Eqns. (2) and (S3)
Δt_{bir}	1 day	Time step for numerical implementation of cell birth in Eqns. (5) and (7)
Δt_{PDE}	0.05 days	Time step for numerical implementation of Eqns. (4), (8), and (S6)
Δt_{record}	1 day	Time step for recording data from model simulations
N_{sim}	Varies	Number of ABM realisations for computing EA cell densities
N_{bin}	Varies	Spatial discretisation step for solving our continuous models
N_{hist}	N_{bin} or 30 voxels	Spatial discretisation step for binning simulations results for comparison

Table 1: Model and simulation parameters used throughout the paper. We note that $N_{bir} \in \{10, 25, 50, 100, 150, 200, 250\}$ realisations for 2D simulations and $N_{bir} \in \{1, 2, 3, 4, 5, 6, 7, 8, 9, 10\}$ realisations for 1D simulations. As we discuss in the SI-§2, $N_{sim} = 5 \times 10^3$ realisations for most EA ABM solutions of the cell-movement model and $N_{sim} = 10^3$ for all EA ABM results of the cell birth and combined models. We set $N_{hist} = 30$ voxels for EA ABM solutions of the cell birth and combined models, and $N_{hist} = N_{bin}$ for the cell-movement model. (See figure captions for our N_{bin} values.) The value of R_{MM} (and R_{XX} , see the SI-§1.3) were reported as repulsion strengths (i.e., R_{MM}/ω_{MM}) in [39].

where the parameters α_{MM} , γ , N_{bir} , and c^+ have the same interpretations as in §2.1 and §2.2. Importantly, by assuming that these parameters have the same interpretations, we are assuming that migration and proliferation are additive, so that combining them has no extra influence. Our fitting approach for these parameters, discussed below, allows us to evaluate this choice and better understand the interplay of these two mechanisms in discrete and continuous settings.

2.4 Parameter estimation procedure

We identify the values of the parameters— α_{MM} in Eqn. (4) and $\{\gamma, c^+\}$ in Eqn. (7)—by minimising the sum of squared differences (hereafter referred to as the “ L^2 error”) between the continuous and EA discrete solu-

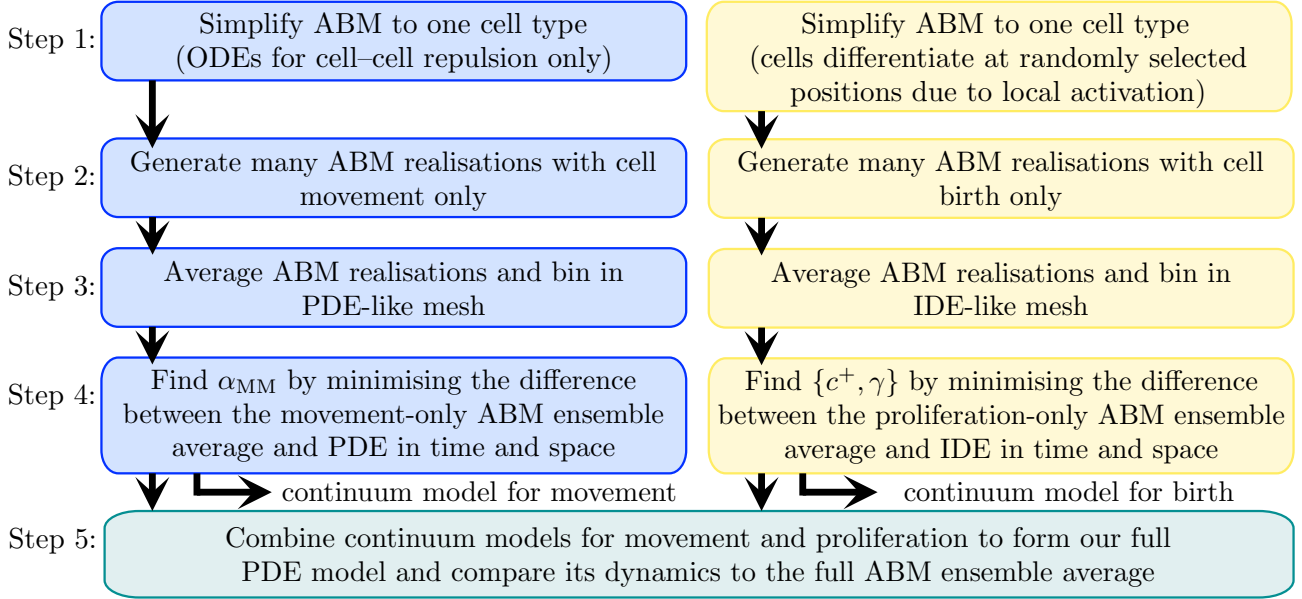


Figure 3: Our modular pipeline for matching the solutions of continuous and discrete models and identifying how cell movement and birth interact in both settings. We first isolate the discrete-model terms from [21] corresponding to movement (left column) and birth (right column) and simplify them to consider only one cell type. We then produce multiple realisations of our ABMs, sorting the cell locations into a grid of $N_{\text{hist}} \times N_{\text{hist}}$ voxels to yield the EA discrete model results. We simulate our continuous model for cell movement (respectively cell birth) and compare it on the same spatial mesh, with values of α_{MM} (respectively c^+ and γ) obtained from a least squares optimisation approach; see the SI-§2 for details. Finally, we combine the fitted movement and birth models to produce our full continuous model. While an extension of this pipeline to fit all three parameters simultaneously is straightforward, fitting separately allows us to better understand the effects of cell movement and birth in discrete and continuous frameworks.

tions over time and space. Because we are able to model the isolated processes of cell birth and movement separately, or consider them acting simultaneously, there are two ways of estimating parameters: by fitting all three parameters simultaneously to data from the combined model, or by fitting them in a modular fashion by considering cell movement and birth in isolation from each other. For the remainder of this paper, we adopt a modular approach because it allows us to probe the particular effects of cell movement and birth in detail (Fig. 3 for an overview), and we present a study of simultaneous estimation in the SI-§3. In particular, by using our modular parameter values in the combined PDE model, we can investigate their interplay and better understand the additive effects of individual-level mechanisms on the accuracy of continuous models. As we discuss in the SI-§3, our modular approach may also supply additional information that can improve parameter estimation. For example, we show in the SI-§3 that α_{MM} and γ are not uniquely identifiable if they are fit only to the combined EA ABM data, whereas Fig. 4(b) and Fig. 7(f) suggest we can uniquely identify them with a modular approach. We overview our method for parameter estimation below; for parameter values, see Table 1. We refer to the SI-§2–§3 for further details about our implementation of the pipeline in addition to alternative choices that could be taken in parameter estimation (such as fitting to earlier times, less refined spatial data, etc.).

We consider biologically meaningful time scales (i.e., days), length scales (i.e., mm), and cell densities and stress empirical units throughout our results. This choice supports future studies that may treat pattern formation with multiple cell types. Throughout our simulations, we consider a domain of size $3 \text{ mm} \times 3 \text{ mm}$ (with one 1D exception in Fig. 7). We implement four initial conditions to extract common features of cell interactions from different geometric scenarios: a square region of melanophores in the centre of the domain (“Box”),

which mimics the symmetry of the domain; a single stripe of melanophores (“Stripe”), which is motivated by the typical patterning observed in wild-type zebrafish; two rectangular regions of melanophores (“Offset rectangles”), which take into account non-standard geometries and the meeting of two disjoint melanophore populations; and two melanophore stripes (“Two stripes”), which explores the interactions between two disjoint melanophore populations with biologically realistic sharp fronts, see Supplementary Fig. 6 for a summary of these initial conditions. We initialise individual ABM simulations by sampling cell positions uniformly in these regions for each respective initial condition, and initialise our continuous models by setting the cell density uniformly equal to the estimated biological density of 400 cells/mm² [21].

In Step 2 of our pipeline in Fig. 3, we solve our discrete models with an explicit approach. Specifically, we solve Eqn. (2) with an explicit forward Euler scheme. To model differentiation from uniformly distributed precursor cells [21], we solve the birth-only ABM by selecting N_{bir} sites in the domain uniformly at random at a fixed time step (here, 1 day) and placing a new cell at each position that meets the conditions given by Eqn. (5). (Following the approach in [21, 39, 40], we evaluate all N_{bir} locations for potential cell proliferation at the same time. This synchronous evaluation means that it is possible, though uncommon, for more than c_{ABM}^+ cells to be present in a local neighborhood, and the choice of parameters in our model, based on the ABMs [21, 39, 40], accounts for this possibility.) We solve our ABM combining migration and birth by simulating Eqn. 2 and then implementing cell birth as above, with migration evaluated using a shorter time step than the time step for birth events.

To compare ABM results directly with the cell density from our continuous models, we obtain an EA distribution by simulating many ABM realisations (here, between 10^3 and 10^4 simulations), sorting all the cell locations into a histogram of $N_{\text{hist}} \times N_{\text{hist}}$ voxels (or $N_{\text{hist}} \times 1$ voxels in 1D), and normalising by the number of simulations and the voxel area for each day simulated; see Step 3 of our pipeline in Fig. 3. Other ways of relating ABM and PDE results are also possible, for example by introducing Gaussian kernels at each cell location [84]. However, as far as the construction of the histogram is concerned, we expect comparable results for particles and localised Gaussian kernels. Furthermore, we show in the SI-§3 that histogram voxel size used to bin EA ABM data and the final time used to fit the continuous equations only play a minor role in affecting the parameter values we obtain, at least for the cell-movement model.

As part of Step 4 of our pipeline in Fig. 3, we need to solve our continuous models, and we do so with explicit approaches. Specifically, we apply a first-order finite volume scheme for the migration model (Eqn. (4)), a forward Euler method for the continuous cell birth model (Eqn. (7)), and a combined finite volume/forward Euler scheme for the full continuous framework (Eqn. (8)). (More details about the particular time steps used to simulate the discrete and continuous models are in the SI-§2.) We simulate the continuous models on an $N_{\text{bin}} \times N_{\text{bin}}$ mesh and, to match with EA ABM solutions, record the average cell density at each day on a (possibly coarser) grid of $N_{\text{hist}} \times N_{\text{hist}}$ voxels.

We compute continuous model parameters by minimising either the L^2 error between the continuous and EA ABM results across time. Notably, this nonlinear least-squares problem is equivalent to maximum likelihood parameter estimation when the densities produced from the ABM simulations are independent, identically distributed normal random variables with constant variance and mean equal to the continuous solution. The L^2 error that we minimise is given by:

$$\begin{aligned}
e_{L^2}^2 &= \|M_{\text{cts}} - M_{\text{ABM}}\|_{L^2}^2 = \int_{t=0}^{t=t_{\text{final}}} \int_{\Omega} (M_{\text{cts}}(\mathbf{x}, t) - M_{\text{ABM}}(\mathbf{x}, t))^2 d\mathbf{x}dt \\
&\approx \Delta t_{\text{record}} \Delta x \Delta y \sum_{n=0}^{N_T} \sum_{i=1}^{N_{\text{hist}}} \sum_{j=1}^{N_{\text{hist}}} (M_{\text{cts},i,j}^{(n)} - M_{\text{ABM},i,j}^{(n)})^2,
\end{aligned} \tag{9}$$

where Δt_{record} denotes the time steps at which data are collected; Δx and Δy are the spatial step sizes of the histogram used to compare the EA ABM and PDE data; $M_{\text{cts},i,j}^{(n)}$ is the continuous-model solution at time t_n and position (x_i, y_j) ; and $M_{\text{ABM},i,j}^{(n)}$ is the corresponding EA ABM result. For the birth-only model we consider fitting

to either the L^2 error as above or simply the difference in the total cell count of the two data sets (we verify in the SI-§2 (Supplementary Table 4) that fitting to the L^2 error produces similar parameter estimates). When we consider cell birth, we simulate our models with different values of N_{bir} and estimate parameters by minimising the sum of the errors across these N_{bir} values. We fit parameters related to cell proliferation sequentially—that is, we determine the optimal value for c^+ before γ . We verify in 1D that sequential and simultaneous estimation does not lead to significant difference in parameter values; see the SI-§3.

3 Results

We now present our results linking discrete and continuous models of cell migration (§2.1), birth (§2.2), and migration and birth (§2.3). We first isolate each interaction process, separately identifying the values of α_{MM} in Eqn. (4) and $\{\gamma, c^+\}$ in Eqn. (7). As we note in §2.4, this choice allows us to extract the distinct effects of each mechanism. We then determine how this simplification affects the ability of the full continuous framework, given by Eqn. (8), to approximate EA ABM solutions. By considering different initial conditions (we discuss the details and motivations for these in the SI-§4), we demonstrate the robustness of our fitting procedure. Our results show how the time scales of proliferation and movement in our continuous model may depend on numerical implementation and the frequency of stochastic cell birth controlled by N_{bir} . Moreover, our modular fitting approach highlights important considerations to account for in more general systems where agents are moving and changing in number.

3.1 Cell migration

We estimate α_{MM} , the scaling parameter that controls the dynamics of melanophore movement. Fig. 4(a) presents the values of α_{MM} that minimise the squared L^2 error between the continuous solution of Eqn. (4) and EA ABM results for our four initial conditions (see §2.4 and the SI-§2–4). In each case, the optimal value of α_{MM} is positively correlated with our PDE mesh resolution, i.e., greater values of α_{MM} are associated with larger $N_{\text{bin}} = N_{\text{hist}}$ values. This unitless parameter appears to converge to around 0.60 to 0.66 as the mesh resolution increases. There is at most a 2.5% relative difference between the values of α_{MM} that we find when $N_{\text{bin}} = 240$ versus when $N_{\text{bin}} = 480$ for our *Box* initial condition. These results suggest that α_{MM} is independent of the mesh resolution when the latter contains at least 240×240 voxels, corresponding to a mesh spacing of $12.5 \mu\text{m}$. As we show in Fig. 2(c), melanophores tend to separate by between $60\text{--}100 \mu\text{m}$ in our ABM results, so this mesh spacing is less than one quarter of the typical distance between agents.

At each mesh resolution in Fig. 4(a), the estimated optimal value of α_{MM} does not appear to depend greatly on the initial condition. For example, in the case of a mesh with $N_{\text{bin}} = N_{\text{hist}} = 240$, the maximum relative difference between the four parameter values is at most 6.5%. This similarity suggests that there is an inherent time scale at which migratory melanophore–melanophore interactions occur. Fig. 4(b), which presents the log L^2 error for $N_{\text{bin}} = 240$ as a function of α_{MM} , further supports this conclusion. Although the errors associated with different initial conditions can vary by an order of magnitude, the minimum value of each (roughly convex) curve appears nearly identical and is located near the values shown in Fig. 4(a).

Fig. 5 presents snapshots of the EA ABM results across 10^4 realisations of Eqn. (2) and the optimised PDE solution associated with the *Box* initial condition. The first row shows the expansion in time of the EA ABM support, i.e., the area occupied by the cells, due to melanophore–melanophore repulsion. For more intuition, we superimpose the cell positions from one ABM realisation on our number-density results in this figure and throughout the manuscript. In all cases, we crop out approximately the upper half of cell positions. Visual inspection of cell positions in Fig. 5 suggests that melanophore–melanophore distances increase near the edge of the collective. Similarly, the speed at which the support expands appears to slow down for the EA ABM result, consistent with melanophores experiencing weaker forces from comparatively distant cells in this region.

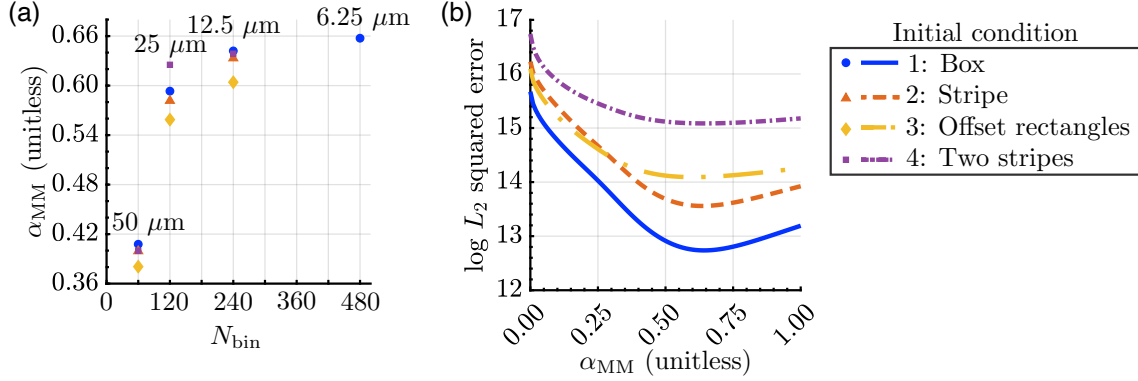


Figure 4: The optimal PDE scaling parameter for movement depends on the mesh resolution but appears to converge. (a) A scatter plot of the numerically optimised value of α_{MM} from Eqn. (4) as a function of the mesh resolution, N_{bin} , demonstrates that this scaling parameter is correlated with the mesh resolution, but appears to converge at sufficiently high (i.e., $N_{bin} \geq 240$) detail. (We omit 95% confidence intervals because these are so narrow that they are difficult to see.) (b) Plotting the $\log L^2$ error, given by Eqn. (9), as a function of α_{MM} with $N_{bin} = 240$ for each initial condition suggests that the values in (a) are optimal. As we show in Fig. 2(c), melanophores are typically separated by more than 60 μm in our movement-only ABM simulations—over four times the voxel width in a grid with $N_{bin} = 240$. See §2.4 and the SI-§2 for numerical details.

We also observe in Fig. 5(a)–(d) that a band of high cell density emerges around the edge of the support which surrounds a ring-like region of low density. These bands may result from the combined effects of cell–cell repulsion and the fine mesh resolution that we use to sort agent positions in the EA solution. Repulsion causes cells at the edge of the collective to travel towards empty regions, while more centrally located agents move more slowly due to the balance of forces from their neighbours. When repulsion separates cells by distances greater than the mesh resolution, we expect regions of low density within the solution support to appear. These oscillatory bands should become less evident when the repulsive potentials in Fig. 1(d) exhibit shallower gradients, as this permits cells to cluster more closely, or when coarser histograms with fewer bins are used to visualise the EA ABM data. As we discuss in the SI-§6, the forces acting on xanthophores are about an order of magnitude smaller than those for melanophores, and we indeed observe less pronounced bands there. Notably, fitting to EA ABM data on coarser histograms lead to similar parameter estimates; see the SI-§3 for details.

We present snapshots of the continuous model, Eqn. (4), under our estimated value of α_{MM} in Fig. 5(e)–(h). This PDE solution captures the dynamics of our example ABM realisation significantly better than the case in Fig. 2(b), when $\alpha_{MM} = 1$. However, unlike the EA ABM result, the PDE does not exhibit bands of high and low cell density. This discrepancy can be further appreciated in Fig. 5(i)–(k), which presents snapshots of the pointwise difference between the PDE and EA ABM solutions. Here positive values indicate that the discrete solution is larger than the continuous one. The lack of bands in the PDE setting is likely because the mean-field assumption used to derive the continuous system is invalid where density is low. We do not expect this discrepancy to be as pronounced in models that include cell birth, as this mechanism increases density; see §3.3. Moreover, the PDE support expands more quickly than that of the ABM. This result is likely due to our choice of error function to fit α_{MM} . Specifically, this parameter is biased towards values that produce accurate approximations in the bulk as these regions have a larger contribution to the L^2 norm. Since we have already determined the assumptions underlying the continuous model break down in low density regions, however, we choose to fit to the bulk of the cell density and focus on the L^2 difference.

To demonstrate that our observations for the *Box* case are consistent across initial conditions, we compare the EA ABM and PDE dynamics for the *Stripe* and *Two stripes* initial conditions in Fig. 6; Supplementary Fig. 7 presents results for the *Offset rectangles* initial condition. In Fig. 6(a)–(d), the column-averaged PDE

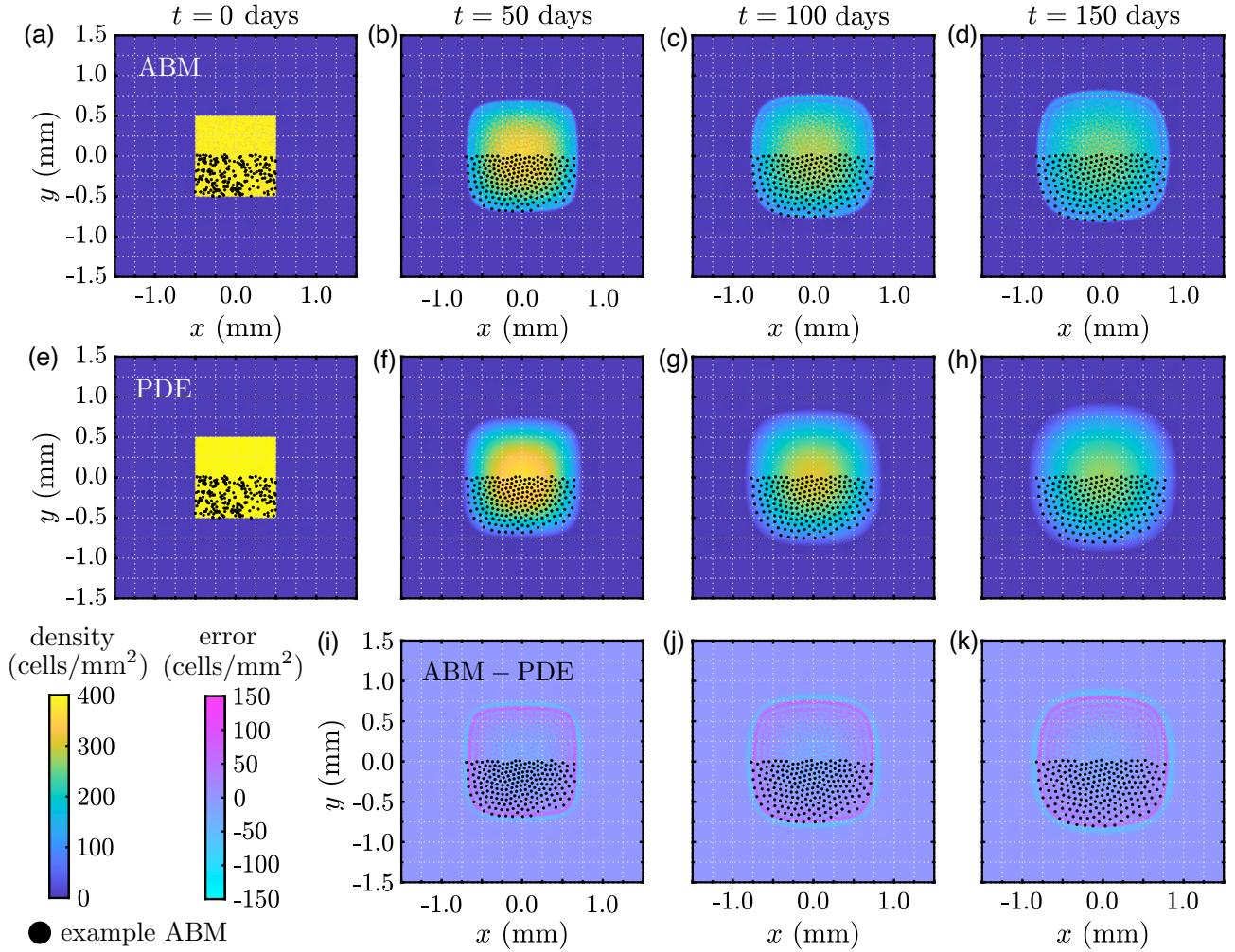


Figure 5: Melanophore movement models with our *Box* initial condition. We present (a)–(d) snapshots of the EA cell density (cells/mm²) across 10⁴ ABM realisations, (e)–(h) the corresponding PDE results using the optimal value of α_{MM} for a mesh resolution of $N_{\text{bin}} = 240$, and (i)–(k) the error between the PDE and EA ABM densities. We overlay cell positions for one example ABM simulation (black points) as a visual guide; we show roughly half of the region occupied by these cells. A difference in cell density of 150 cells/mm² in a given voxel corresponds to about 0.0234 cells for this choice of mesh resolution. We find that the average pointwise errors (over voxels where at least one of the EA ABM or PDE solutions is non-zero) are about 28 cells/mm², 17 cells/mm², 17 cells/mm², and 17 cells/mm² at $t = 0, 50, 100,$ and 150 days, respectively. (These values correspond, respectively, to roughly 7%, 4%, 4%, and 4% of the maximum cell density of 400 cells/mm²).

solution, i.e., the solution average over the x variable, has a larger support than that of the EA ABM and does not exhibit oscillatory bands. (Comparing column averages is justified because both results are nearly uniform along the x -axis.) Nevertheless, the continuous solution closely approximates the EA ABM density, particularly in regions where the latter is high. For example, we find that the average pointwise error (over voxels where at least one of the EA ABM or PDE solution is non-zero) is equal to about 40 cells/mm² at $t = 0$ days, 24 cells/mm² at $t = 50$ days, 23 cells/mm² at $t = 100$ days, and 23 cells/mm² at $t = 150$ days (these correspond to roughly 10%, 6%, 6%, and 6% of the maximum cell density of 400 cells/mm², respectively). Both solutions invade empty space in time, and the speed of this travelling wavefront appears to slow as cells become more diffuse. For the *Two stripes* initial condition in Fig. 6(e)–(h), the ABM and PDE predict that cells move into

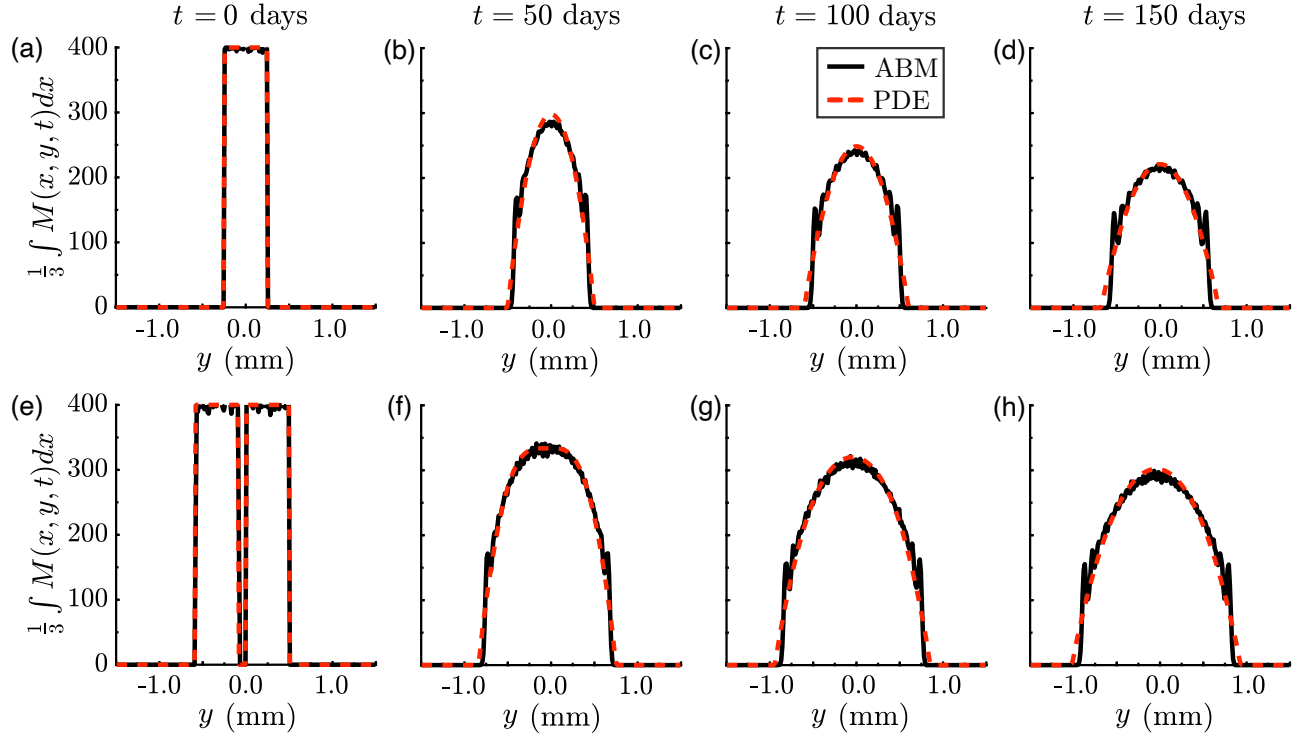


Figure 6: Melanophore movement models with our *Stripe* and *Two stripes* initial conditions. (a)–(d) We present snapshots of the column-averaged cell density (cells/mm², black solid line), generated from 10^3 ABM realisations for the *Stripe* case, alongside the corresponding PDE solution (dashed red line) under a mesh resolution of $N_{\text{bin}} = 240$ and our optimised value of α_{MM} . (e)–(f) Similarly, we show snapshots of the column-averaged density, generated from 10^3 ABM realisations for the *Two stripes* case, and the corresponding PDE solution. The 2D solutions are nearly uniform in the x -direction (data not shown).

the initially empty space between stripes to approach a characteristic profile also observed in the one-stripe case. The EA ABM model does not appear to form oscillatory bands in the interstripe region, corroborating our hypothesis that these bands are more likely to arise near the edge of the solution support. In this case, the average pointwise error between the continuous and discrete data is roughly 18%, 11%, 11% and 11% of the maximum cell density at $t = 0, 50, 100,$ and 150 days, respectively.

3.2 Cell birth

We identify the density-limiting parameter c^+ and growth rate γ in our IDE model, Eqn. (7), by comparing with agent-based data from Eqn. (5). Importantly, the dynamics of discrete-model proliferation, unlike cell migration, involve stochasticity beyond the initial condition. To gain intuition, we thus start with 1D simulations: for each value of $N_{\text{bir}} \in \{1, 2, \dots, 10\}$, we compute the EA of 10^3 ABM realisations from an initial condition in which a single melanophore is placed at the origin in a 1D domain. In Fig. 7(a) we show the EA result for $N_{\text{bir}} = 1$ and the corresponding IDE model solution with the optimal values of γ and c^+ in Fig. 7(b). The continuous solution appears to have a smaller radius of support than the EA ABM result at every time point; see Fig. 7(c). This result holds across all N_{bir} values in Fig. 7(d). While the IDE predicts a piecewise linear growth of the total number of cells, the corresponding EA ABM result increases linearly before slowly saturating as the domain fills, as we depict in Fig. 7(e). This behaviour likely arises from our overcrowding condition that prevents cell densities from exceeding c^+ . As the domain fills with cells, it becomes less likely to select a location \mathbf{z} that satisfies the overcrowding condition in the ABM. This reduces the population growth rate at later

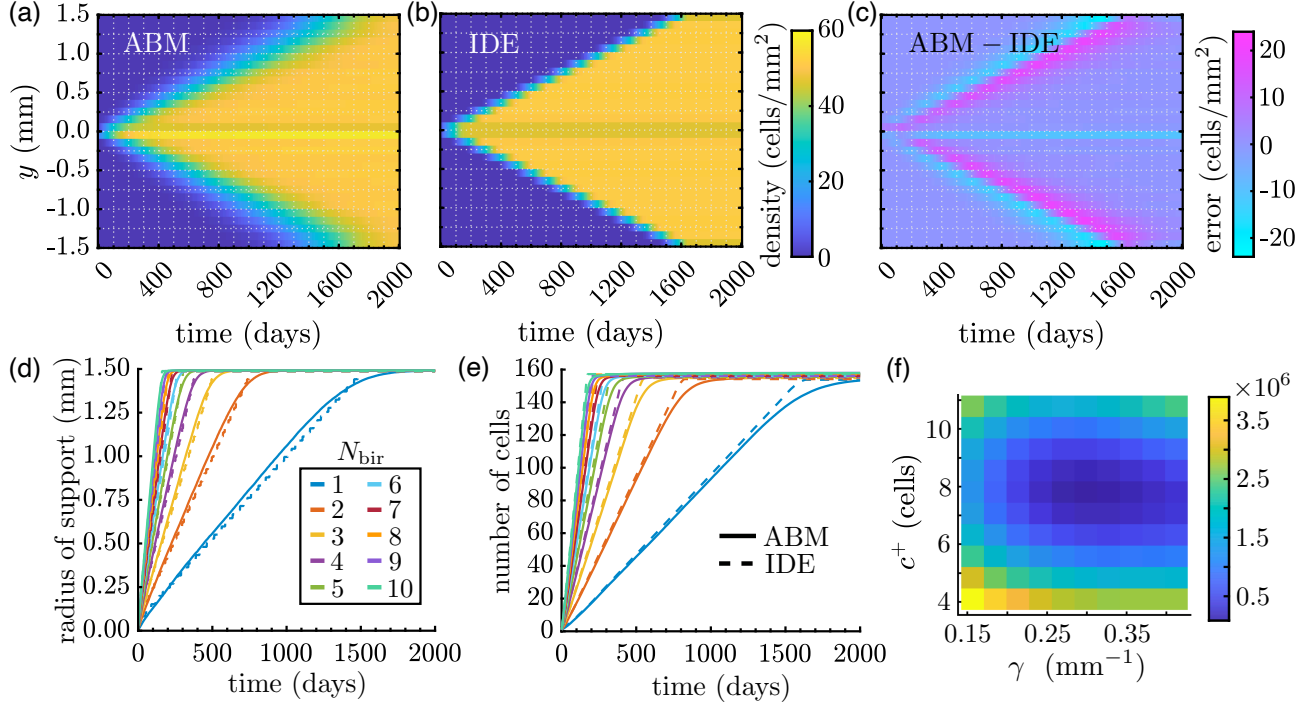


Figure 7: Melanophore birth models with a baseline initial condition of one cell at $y = 0$ in a 1D domain. Results in (a)–(c) are for $N_{\text{bir}} = 1$ position/day. (a) We compute the EA ABM result by simulating 10^3 realisations of our ABM birth model, Eqn. (5), and binning cell positions in a histogram with 0.1 mm-wide voxels (i.e., $N_{\text{hist}} = 30$). (b) We use a finer mesh resolution to solve our corresponding IDE model (Eqn. (7)) before transferring results to the same histogram in (a) to perform parameter estimation. Here we show our IDE solution produced with optimal parameter values $c^+ = 7.592$ cells and $\gamma = 0.2822$. (c) The difference between our discrete and continuous results highlights that the ABM support is wider than the PDE support. (d) This is also visible by comparing their mean radii of support in time. To compute the mean radius of support for the ABM at a given time, we find the most distant melanophore from $y = 0$ for each simulation and average across these values. (e) Cell mass grows linearly in both models at first, but stochastic effects coupled with our overcrowding condition drive down the growth rate of the ABM as the domain fills with cells. (f) Plotting the squared L^2 space-time difference between the discrete and continuous densities, summed over all N_{bir} values considered (namely $N_{\text{bir}} = 1, \dots, 10$), as a function of the density-limiting parameter c^+ and birth-rate scaling parameter γ highlights its convex shape in c^+ and lesser sensitivity to γ . We compute this L^2 difference using a time step of 10 days here, and our results are based on 10^3 simulations for each N_{bir} value; see the SI-§3 for parameter values under alternative choices in our estimation process.

times. In contrast, the IDE model specifies that the support increases by the same amount at each time step until it reaches the domain boundaries. As we discuss in §4, capturing discrete model behaviour more accurately at higher cell numbers may require replacing γ in our IDE with a density-dependent function.

Our 1D simulations provide a baseline case to test our estimation process. As we note in §2.4, we employ a sequential procedure, first fitting c^+ with $\gamma = |\Omega|^{-1}$ and then estimating γ with c^+ fixed. In the 1D case, this leads to optimal values $c^+ = 7.592$ cells and $\gamma = 0.2822$. If we instead estimate both parameters simultaneously, we find $c^+ = 7.430$ cells and $\gamma = 0.2902$. This is a difference of about 2.1% in c^+ and 2.8% in γ , suggesting that sequential estimation reduces computational complexity without strongly affecting parameter values. To understand if a coarser discrepancy measure based only on cell numbers at each time is sufficient, we also fit c^+ and γ by minimising the squared difference in the total cell numbers over time; see the SI-§2, Supplementary Table 4 for the resulting parameter values. The corresponding parameter estimates differ from the density-based

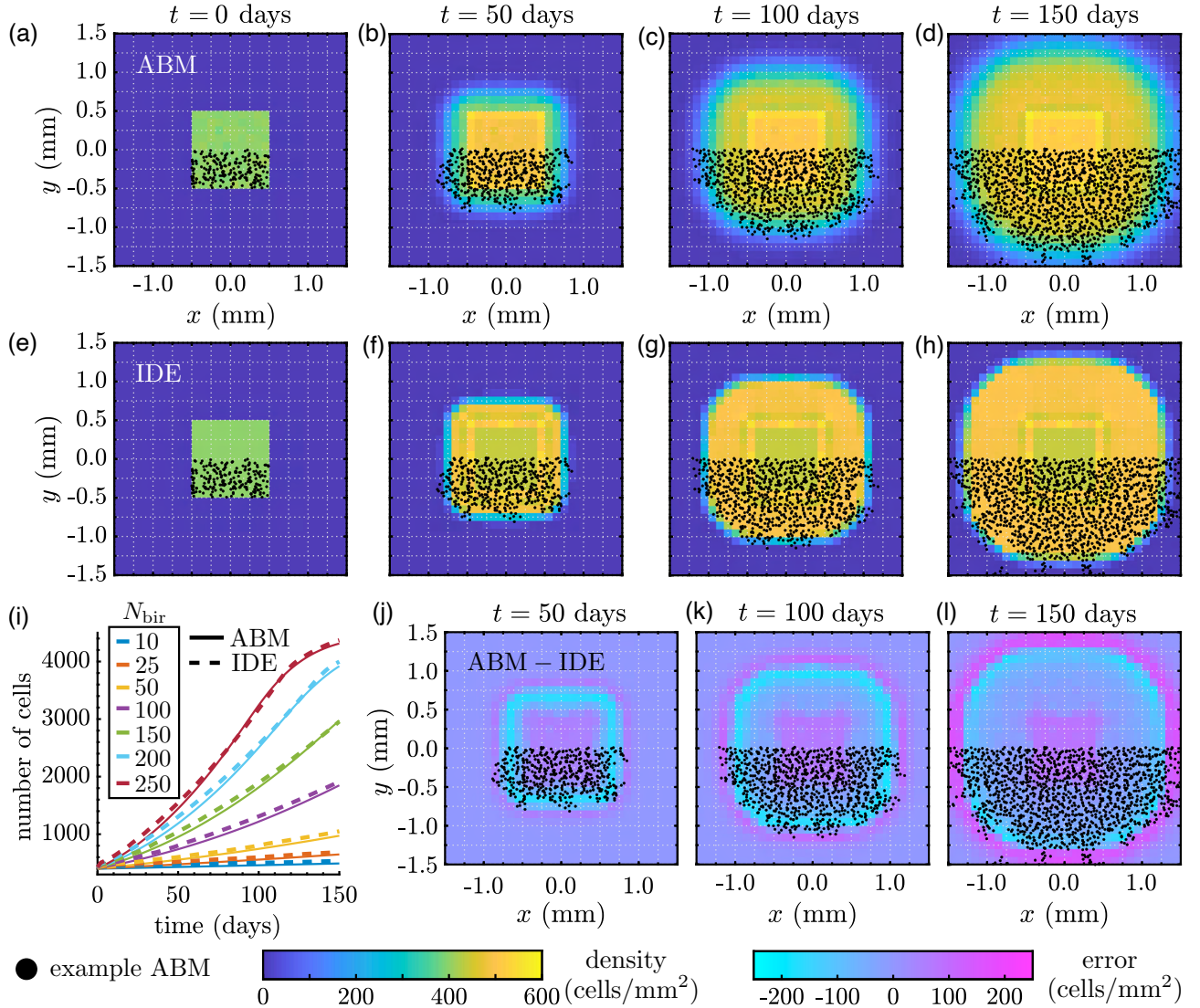


Figure 8: Melanophore proliferation models with our *Box* initial condition. Results in (a)–(h) and (j)–(l) are for $N_{\text{bir}} = 150$ positions/day. We compute (a)–(d) the EA ABM result across 10^3 simulations, and (e)–(h) the solution of our IDE model with optimal parameters $c^+ = 8.564$ and $\gamma = 0.1274$. (i) Our continuous model captures the mean number of cells in our ABM simulations for different N_{bir} values well across time. (j)–(l) As in the 1D case in Fig. 7, the difference between the IDE and EA ABM results demonstrates that the ABM support extends beyond the IDE support. To provide more intuition, we overlay roughly half of the cell positions from an example ABM simulation in (a)–(h) and (j)–(l). See Supplementary Fig. 8 and Supplementary Table 4 for corresponding simulations using our *Offset rectangles* initial condition.

case by approximately 1.2% for c^+ and γ , suggesting both error measures are reasonable. Both approaches also appear to exhibit similar sensitivity as parameters are varied (compare Figs. 7(f) and Supplementary Fig. 2).

Fig. 8 and Supplementary Fig. 8, respectively, show that proliferation in 2D broadens the solution support from the *Box* and *Offset rectangles* initial conditions over time, and the IDE model accurately captures the total cell mass of the ABM system for all N_{bir} values considered. Our estimated optimal values of c^+ and γ for these two initial conditions differ by about 2.5% and 0.31%, respectively, suggesting that our estimation procedure is robust to the initial condition. We also highlight that a region of higher density forms at the edge of the initial condition’s support for both the ABM and IDE in Fig. 8(a)–(h). Indeed, if \mathbf{z} is near the support boundary,

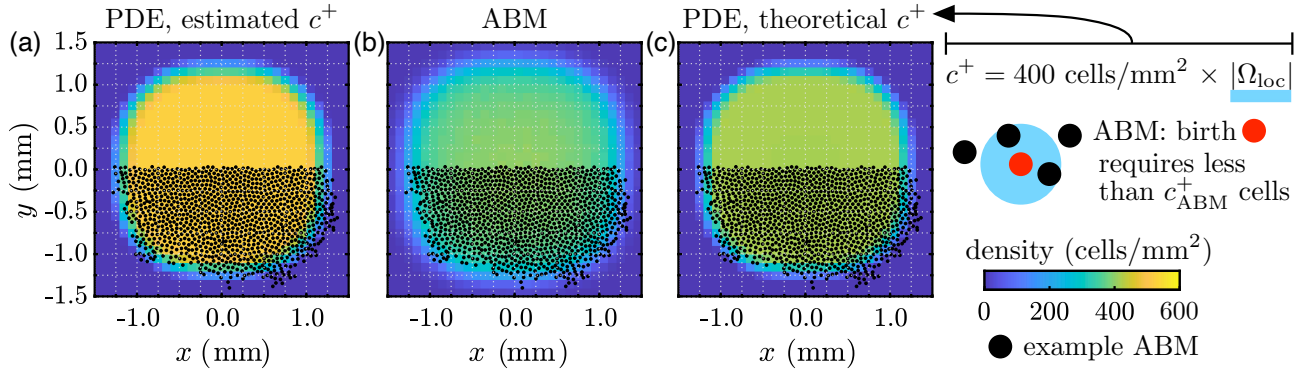


Figure 9: A modular approach to fitting parameters for cell movement and birth does not account for the interplay between these two mechanisms. We show results in (a)–(c) at $t = 100$ days for $N_{\text{bir}} = 150$ positions/day. (a) The solution of our full PDE model (Eqn. (8)) with the values of α_{MM} and $\{c^+, \gamma\}$ that we fit based on ABM simulations of cell movement and birth, respectively, captures the support of the ABM EA result, but not its density. (b) In comparison, the density for the full discrete model is roughly 400 cells/mm². (c) By integrating this density, which is based on empirical estimates of melanophore–melanophore distances [21, 82], over an Ω_{loc} -region, we find that $c^+ \approx 7.0686$ cells. With this value of c^+ , alongside the values of α_{MM} and γ that we estimated for migration and birth individually, our PDE produces cell densities that more accurately represent the ABM dynamics.

Ω_{loc}^z covers only a fraction of the occupied domain, thereby meeting both conditions for birth. Conversely, the cell density at the centre of the domain is comparatively low throughout time because the total number of cells contained within disks of size $|\Omega_{\text{loc}}|$ is already close to the threshold c^+ . Interestingly, as in the 1D case with only proliferation, the ABM EA support is larger than that of the IDE solution, the reverse of the behaviour that we observed for cell migration in Fig. 5.

3.3 Cell movement and proliferation

To obtain a full continuous model, we may substitute our estimated values of the migration scaling parameter α_{MM} , density-limiting parameter c^+ , and birth-rate scaling parameter γ into Eqn. (8). However, comparing this model to the dynamics of our full ABM shows that migration and proliferation have interwoven effects. To illustrate this phenomenon, we present a PDE solution with our optimal values of α_{MM} , c^+ , and γ from §3.1 and 3.2 at $t = 70$ days in Fig. 9(a). We observe that this PDE model produces a significantly higher cell density than its discrete counterpart in Fig. 9(b). This discrepancy occurs regardless of the value of N_{bir} , which influences the speed of cell birth. Related to this, we notice that the long-time cell density in our ABM results is much lower when both mechanisms operate simultaneously than it is when only birth occurs; compare Fig. 8(d) and Fig. 9(b). On the other hand, the inclusion of movement does not influence the long-time density of the continuous model solution; see the colourbar in Fig. 8(h) in comparison to the one in Fig. 9. Although we do not furnish these observations with an analytical explanation here, they demonstrate an interesting difference in how “adding” mechanisms or terms impact PDE and ABM dynamics.

One approach to addressing these discrepancies is to refit all three scaling parameters (α_{MM} , γ , and c^+) simultaneously, and we present the results of this approach in the SI-§3. (Indeed, we show there that the errors produced with a simultaneous estimation approach can be relatively small, although the model parameters may not all be identifiable.) Because we are interested in understanding the interplay of individual-based mechanisms of proliferation and movement in continuous models, however, we instead take a simpler theoretical approach. Namely, we notice that the parameter c^+ is largely responsible for controlling the maximum cell density over long time periods. (We determine this by integrating Eqn. (8) over space and identifying the steady-state

dynamics; this analysis reveals that equilibrium is reached when the density within any neighborhood Ω_{loc}^x is below c^+ .) In order to limit the maximum density to our estimated empirical value of 400 cells/mm² [21, 82], we let $c^+ = 400|\Omega_{\text{loc}}| \approx 7.0686$ cells. As we show in Fig. 9(c), using this value of c^+ , alongside our previously fit values of α_{MM} and γ , produces PDE densities that are much closer to the corresponding ABM results. We thus fix $c^+ = 7.0686$ cells for the remainder of this manuscript, which allows us to highlight the time dynamics of our full PDE model in comparison to the EA ABM result with *Box* and *Offset rectangles* initial conditions in Fig. 10 and 11, respectively.

Fig. 10(j), which depicts the time evolution of the estimated radius of support for the PDE and EA ABM results, shows that a reasonably accurate continuous description of the combined model can be obtained by using the scaling parameters obtained from a modular approach. The supports of the ABM and PDE solutions both increase at roughly the same rate, although the degree to which the solutions agree can be affected by N_{bir} : when this parameter is small, the PDE solution travels at a faster rate than the ABM solution, whereas the opposite occurs when this value is large (greater than $N_{\text{bir}} = 50$ positions/day). At intermediate values of N_{bir} (i.e., $N_{\text{bir}} = 50$ positions/day), however, the ABM and PDE solution curves are almost identical. Fig. 10(i), which presents the number of cells over time, yields similar observations: the ABM and PDE solutions exhibit similar dynamics over the time period investigated here and there are certain values of N_{bir} for which the solution curves are nearly identical. Fig. 11 further demonstrates that these observations do not depend on the specific choice of initial condition. Figs 10 and 11 demonstrate that combining movement with proliferation also dissipates the oscillatory bands that we observed for movement alone in Fig. 5. This is likely because the stochastic addition of cells in the birth model disrupts the regular cell spacing created by the movement model. Furthermore, the EA ABM and PDE solutions exhibit similar characteristic profiles without regions of high cell density around the edge of the initial condition support, in contrast to the birth-only model (Fig. 8).

4 Discussion

We presented a procedure for constructing experimentally interpretable continuous models of cell migration and birth in biologically relevant settings of low numbers of individuals and localised interactions which may lie outside the validity of the mean-field regime. Specifically, we introduced and estimated scaling parameters in continuous models to account for realistic—i.e., relatively small and changing—numbers of cells with localised interactions. We applied this methodology to an illustrative, simplified example inspired by zebrafish pattern formation, in which we used a reduced ABM to generate individual-level data with biologically meaningful spatial and temporal units. Non-local rules for cell birth and migration, based on the ABM [21], informed our discrete and continuous descriptions and allowed us to transfer biological length scales and units to the macroscopic setting. Throughout our work, we stressed matching the spatio-temporal behaviour of our continuous and discrete models. We adopted a modular approach by estimating parameters in cases with either movement or birth before considering both mechanisms simultaneously. This allowed us to examine the specific contributions of each mechanism to self-organisation and provided insight into their interplay in discrete and continuous settings.

We observed that the solutions of our continuous models expand at a different rate than EA ABM results and feature smoother profiles. Indeed, inaccuracies in mean-field descriptions for “intermediate” numbers of individuals appear to be common in other biological phenomena described by simpler dynamics such as Fisher-KPP-type equations, cf. [85, 86]. In fact, both references analytically derive corrections to the wave speed, a procedure we cannot adopt due to our use of off-lattice models. However, this substantiates our introduction of scaling parameters to handle the discrepancy. By introducing and estimating parameters that rescale the time variable, we produced more accurate descriptions of agent-based movement or birth. However, when we used the same parameter values in a continuous model of both cell migration and birth in §3.3, the PDE did not produce close estimates of the full ABM. Specifically, our full continuous model yielded larger long-time densities than the EA ABM results, motivating us to re-estimate the threshold value c^+ with a

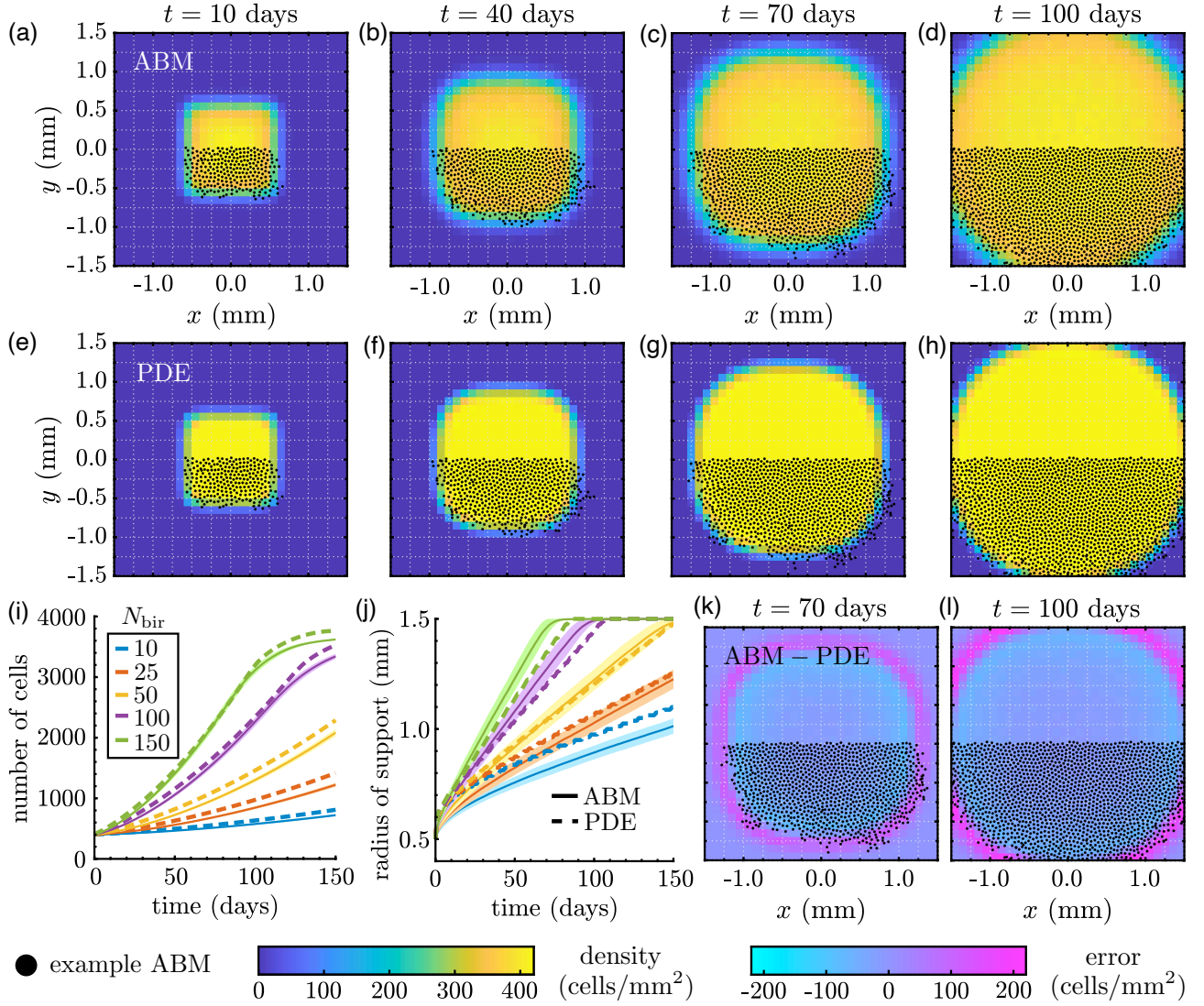


Figure 10: Melanophore movement and birth models with our *Box* initial condition. Results in (a)–(h) and (j)–(l) are for $N_{\text{bir}} = 150$ positions/day. We (a)–(d) compute the EA ABM result using 10^3 simulations, and (e)–(h) generate the PDE solution of Eqn. (8) with $c^+ = 7.0686$ cells and the values of α_{MM} and γ that we estimated in §3.1 and §3.2, respectively. (i) The time evolution of the PDE cell mass agrees well with the mean number of cells for the ABM under different N_{bir} values. (j) Depending on the time scales of migration and birth, the approximate PDE radius of support overtakes or trails the corresponding EA ABM result. We compute the radius of support for each ABM realisation by finding the most distant cell from the origin at each time step; we then average these values across our simulations. In the PDE case, we find the furthest voxel with non-zero density from the origin based on the L^∞ distance, after setting the density to zero if it is below single-digit precision of 10^{-7} . (k)–(l) We show the difference between the PDE and EA ABM solutions from (a)–(h) at two sample times. We overlay cell positions from one ABM simulation to illustrate how the continuous and discrete solutions are related. In (i) and (j), shaded regions denote plus or minus one standard deviation of the EA ABM solution.

theoretical approach. This generated a more faithful continuous description and highlighted that the effects of movement and proliferation are not simply additive. We thus stress that parameters must be fit to data in which all mechanisms of interest act simultaneously, in order to capture their interplay. This is particularly crucial for

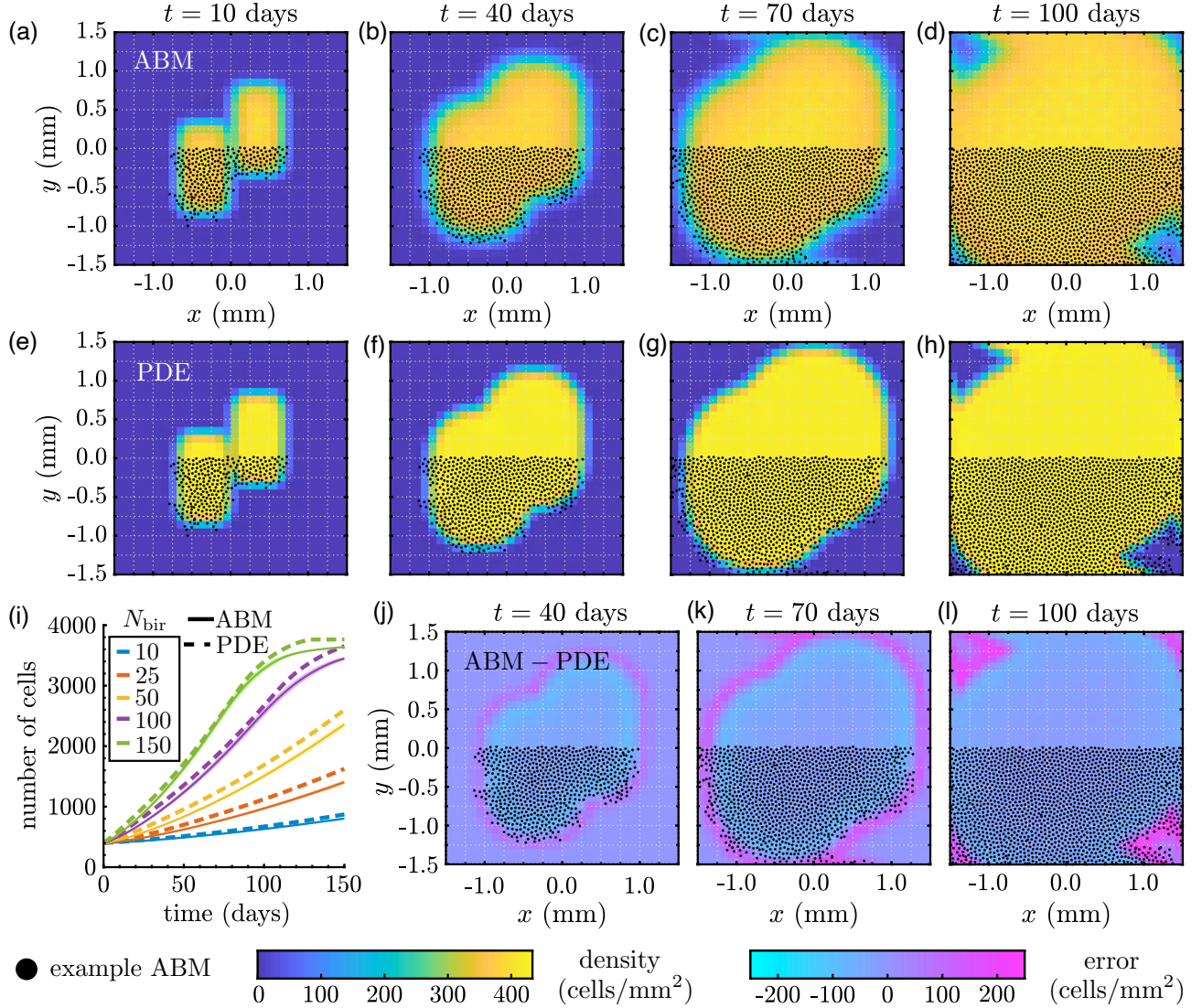


Figure 11: Melanophore movement and birth models with our *Offset rectangles* initial condition to verify that our fitting procedure is robust in non-standard geometries. Results in (a)–(h) and (j)–(l) are for $N_{\text{bir}} = 150$ positions/day. As in Fig. 10, we show (a)–(d) the EA ABM result across 10^3 simulations; (e)–(h) the corresponding PDE solution with $c^+ = 7.0686$ cells and the values of α_{MM} and γ that we estimated in §3.1 and §3.2, respectively; (i) the PDE cell mass in time compared to the mean number of cells across 10^3 ABM simulations for different N_{bir} values; and (j)–(l) the difference between the PDE and EA ABM solutions from (a)–(h). To provide more intuition, we overlay some cell positions from one ABM simulation.

contexts such as cancer biology, where cell migration, proliferation, and death are known to play critical roles in tumour progression and immune response [87].

Our results highlight how choices in numerical implementation affect parameter estimates and suggest several directions for future work that may improve our approach. For example, the optimal value of our parameter controlling the timescale of cell migration (α_{MM}) appears to be independent of the initial condition and the mesh resolution that we used to construct PDE solutions, provided the latter is sufficiently refined. One drawback of our current approach, however, is that we may need to estimate α_{MM} and γ for each new choice of discrete rules governing migration and cell birth, respectively, because these rules perturb the short-range interactions between relatively small numbers of cells. This naturally leads to the question of whether

an analytic expression can be derived for these parameters. Several coarse-graining techniques that take into account higher-order correlations between cells in on- or off-lattice models may produce scaling factors similar to those introduced in this manuscript, but these may only apply to certain classes of ABMs [88]. Alternatively, it may be possible to estimate scaling parameters of continuous models by investigating the convergence of EA ABM results to features of their solutions such as the speed of solution propagation, as in [85, 86] for on-lattice models; by accounting for the dynamics of the two-particle distribution, as in [73, 74]; or by exploring scaling relationships as in [89]. Adapting these approaches to our setting is an interesting avenue for future work.

Additionally, our continuous models more accurately represent ABM results within the bulk of the solution support because the L^2 norm more strongly penalises discrepancies there. In the future, other norms, such as the L^∞ error, could be used to match the solution supports given by our discrete and continuous models. Replacing our birth-rate scaling parameter γ with a density-dependent function—either through rigorous derivation or an equation-learning approach [90]—is another exciting future direction. In particular, because cell proliferation in the ABM involves selecting positions uniformly at random from the domain each day, the chance that we select a location \mathbf{z} that permits birth appears to depend in a nonlinear way on the solution support. More generally, our computational study does not provide theoretical explanations for our parameter values, and we plan to build on the intuition that we established here to develop these arguments in the future.

To simplify our initial study, we considered the dynamics of one cell population (i.e., melanophores in the main text and xanthophores in the SI-§6), but pattern formation in zebrafish skin involves multiple cell types and longer-range interactions, as we highlight in Supplementary Fig. 1. Future work may extend our pipeline to construct more realistic continuous models with multiple cell types and interaction neighborhoods. Related to this, the initial conditions that we designed allowed us to make one-to-one comparisons between discrete- and continuous-model densities, but this may not always be possible. More realistic zebrafish models (i.e., [21, 37, 39, 40]) produce patterns that are more complicated than our box and stripe motifs. This means that ensemble-averaging stochastic ABM realisations may not retain information about the length scales inherent in patterns. For such cases, fitting parameters based on summary statistics (e.g., pair-correlation functions [91], pattern-simplicity scores [92], or persistent-homology approaches [93]) may be more useful, and we plan to address this in future work. These and other directions move us toward constructing interpretable, analytically tractable continuous models of self-organisation, increasing our understanding of biological pattern formation more broadly.

Code availability

Our model and parameter-fitting code is publicly available on GitHub [94]. Supplementary figures and videos are available on Figshare at https://figshare.com/projects/Linking_discrete_and_continuous_models_of_cell_birth_and_migration_in_one_population/171234. Data used to generate figures are given in Dryad <https://datadryad.org/stash/share/ErRoj5orc7qjK2NuuKSp3rWJvNz6QPLSNhPlm1052BU>.

Acknowledgements

JAC and WDM were supported by the Advanced Grant Nonlocal-CPD (Nonlocal PDEs for Complex Particle Dynamics: Phase Transitions, Patterns and Synchronization) of the European Research Council Executive Agency (ERC) under the European Union’s Horizon 2020 research and innovation programme (grant agreement No. 883363). WDM, JAC, and AV would also like to thank the Isaac Newton Institute for Mathematical Sciences, Cambridge, for support and hospitality during the programme Mathematics of Movement, where work on this paper was undertaken. This work was supported by EPSRC grant no EP/R014604/1. CV acknowledges support from the Dr Perry James (Jim) Browne Research Centre on Mathematics and its Applications (University of Sussex). We are grateful to Shigeru Kondo for helpful discussions during an early stage of this research.

References

- [1] Mogilner A, Edelstein-Keshet L. A non-local model for a swarm. *J Math Biol.* 1999;38(6):534-70.
- [2] D’Orsogna MR, Chuang YL, Bertozzi AL, Chayes LS. Self-propelled particles with soft-core interactions: patterns, stability, and collapse. *Phys Rev Lett.* 2006;96(10):104302.
- [3] Cucker F, Smale S. Emergent behavior in flocks. *IEEE Trans Autom Control.* 2007;52(5):852-62.
- [4] Carrillo JA, Fornasier M, Toscani G, Vecil F. Particle, kinetic, and hydrodynamic models of swarming. In: *Mathematical modeling of collective behavior in socio-economic and life sciences.* Springer; 2010. p. 297-336.
- [5] Amack JD, Manning ML. Knowing the boundaries: Extending the differential adhesion hypothesis in embryonic cell sorting. *Science.* 2012;338:212-5.
- [6] Burger M, Francesco MD, Fagioli S, Stevens A. Sorting phenomena in a mathematical model for two mutually attracting/repelling species. *SIAM J Math Anal.* 2018;50(3):3210-50.
- [7] Carrillo JA, Murakawa H, Sato M, Togashi H, Trush O. A population dynamics model of cell-cell adhesion incorporating population pressure and density saturation. *J Theor Biol.* 2019;474:14-24.
- [8] Buttenschön A, Edelstein-Keshet L. Bridging from single to collective cell migration: A review of models and links to experiments. *PLOS Comput Biol.* 2020;16(12).
- [9] Tsai TYC, Garner RM, Megason SG. Adhesion-Based Self-Organization in Tissue Patterning. *Annu Rev Cell Dev Biol.* 2022;38:349-74.
- [10] Frohnhöfer HG, Krauss J, Maischein HM, Nüsslein-Volhard C. Iridophores and their interactions with other chromatophores are required for stripe formation in zebrafish. *Development.* 2013;140(14):2997-3007.
- [11] Irion U, Nüsslein-Volhard C. The identification of genes involved in the evolution of color patterns in fish. *Curr Opin Genet Dev.* 2019;57:31-8.
- [12] Parichy DM. Evolution of pigment cells and patterns: recent insights from teleost fishes. *Curr Opin Genet Dev.* 2021;69:88-96.
- [13] Kondo S, Watanabe M, Miyazawa S. Studies of Turing pattern formation in zebrafish skin. *Philos Trans R Soc A.* 2021;379(2213):20200274.
- [14] Nakamasu A, Takahashi G, Kanbe A, Kondo S. Interactions between zebrafish pigment cells responsible for the generation of Turing patterns. *Proc Natl Acad Sci USA.* 2009;106(21):8429-34.
- [15] Singh AP, Schach U, Nüsslein-Volhard C. Proliferation, dispersal and patterned aggregation of iridophores in the skin prefigure striped colouration of zebrafish. *Nat Cell Biol.* 2014;16(6):604-11.
- [16] Gur D, Bain EJ, Johnson KR, Aman AJ, Amalia Pasolli H, Flynn JD, et al. In situ differentiation of iridophore crystallophenotypes underlies zebrafish stripe patterning. *Nat Commun.* 2020;11(1):6391.
- [17] Hamada H, Watanabe M, Lau HE, Nishida T, Hasegawa T, Parichy DM, Kondo S. Involvement of Delta/Notch signaling in zebrafish adult pigment stripe patterning. *Development.* 2014;141(2):318-24.
- [18] Inaba M, Yamanaka H, Kondo S. Pigment pattern formation by contact-dependent depolarization. *Science.* 2012;335(6069):677-7.

- [19] Yamaguchi M, Yoshimoto E, Kondo S. Pattern regulation in the stripe of zebrafish suggests an underlying dynamic and autonomous mechanism. *Proc Natl Acad Sci USA*. 2007;104(12):4790–4793.
- [20] Kroll F, Powell GT, Ghosh M, Gestri G, Antinucci P, Hearn TJ, et al. A simple and effective F0 knockout method for rapid screening of behaviour and other complex phenotypes. *eLife*. 2021;10:e59683.
- [21] Volkening A, Sandstede B. Modelling stripe formation in zebrafish: an agent-based approach. *J R Soc Interface*. 2015;12(112):20150812.
- [22] Fadeev A, Krauss J, Frohnhöfer HG, Irion U, Nüsslein-Volhard C. Tight Junction Protein 1a regulates pigment cell organisation during zebrafish colour patterning. *eLife*. 2015;4:e06545.
- [23] Byrne HM. Dissecting cancer through mathematics: From the cell to the animal model. *Nat Rev Cancer*. 2010;10:221-30.
- [24] Gompper G, Winkler RG, Speck T, Solon A, Nardini C, Peruani F, et al. The 2020 motile active matter roadmap. *J Phys Condens Matter*. 2020;32:193001.
- [25] Stillman NR, Mayor R. Generative models of morphogenesis in developmental biology. *Semin Cell Dev Biol*. 2023;147:83-90.
- [26] Volkening A. Linking genotype, cell behavior, and phenotype: multidisciplinary perspectives with a basis in zebrafish patterns. *Curr Opin Genet Dev*. 2020;63:78-85.
- [27] Alert R, Trepast X. Physical models of collective cell migration. *Annu Rev Condens Matter Phys*. 2020;11:77-101.
- [28] Metzcar J, Wang Y, Heiland R, Macklin P. A review of cell-based computational modeling in cancer biology. *JCO Clin Cancer Inform*. 2019;2:1-13.
- [29] Deutsch A. Cellular automaton models for collective cell behaviour. In: *Cellular Automata and Discrete Complex Systems. AUTOMATA 2015. Lecture Notes in Computer Science*. Springer; 2015. p. 1-10.
- [30] Deutsch A, Dormann S. *Cellular Automaton Modeling of Biological Pattern Formation, Characterization, Examples, and Analysis*. Springer; 2017.
- [31] Hirashima T, Rens EG, Merks RMH. Cellular Potts modeling of complex multicellular behaviors in tissue morphogenesis. *Dev Growth Differ*. 2017;59(5):329-39.
- [32] Rens EG, Edelstein-Keshet L. From energy to cellular forces in the Cellular Potts Model: An algorithmic approach. *PLOS Comput Biol*. 2019;15(12):1-23.
- [33] Alt S, Ganguly P, Salbreux G. Vertex models: from cell mechanics to tissue morphogenesis. *Philos Trans R Soc B*. 2017;372(1720):20150520.
- [34] Fletcher A, Osterfield M, Baker R, Shvartsman S. Vertex Models of Epithelial Morphogenesis. *Biophys J*. 2014;106(11):2291-304.
- [35] Bullara D, De Decker Y. Pigment cell movement is not required for generation of Turing patterns in zebrafish skin. *Nat Commun*. 2015;6(6971).
- [36] Moreira J, Deutsch A. Pigment pattern formation in zebrafish during late larval stages: A model based on local interactions. *Dev Dyn*. 2005;232(1):33-42.
- [37] Owen JP, Kelsh RN, Yates CA. A quantitative modelling approach to zebrafish pigment pattern formation. *eLife*. 2020;9:e52998.

- [38] Caicedo-Carvajal CE, Shinbrot T. In silico zebrafish pattern formation. *Dev Biol.* 2008;315(2):397-403.
- [39] Volkening A, Abbott MR, Chandra N, Dubois B, Lim F, Sexton D, Sandstede B. Modeling stripe formation on growing zebrafish tailfins. *Bull Math Biol.* 2020;82(56).
- [40] Volkening A, Sandstede B. Iridophores as a source of robustness in zebrafish stripes and variability in *Danio* patterns. *Nat Commun.* 2018;9(3231).
- [41] Osborne JM, Fletcher AG, Pitt-Francis JM, Maini PK, Gavaghan DJ. Comparing individual-based approaches to modelling the self-organization of multicellular tissues. *PLOS Comput Biol.* 2017;13:e1005387.
- [42] Murray JD. *Mathematical biology: I. An introduction.* Springer; 2002.
- [43] Perthame B. *Transport equations in biology.* Springer Science & Business Media; 2006.
- [44] Turing AM. The chemical basis of morphogenesis. *Philos Trans R Soc Lond B.* 1952;237(641):37-72.
- [45] Maini P, Painter K, Chau HP. Spatial pattern formation in chemical and biological systems. *J Chem Soc.* 1997;93(20):3601-10.
- [46] Marciniak-Czochra A, Karch G, Suzuki K. Instability of Turing patterns in reaction-diffusion-ODE systems. *J Math Biol.* 2017;74:583-618.
- [47] Armstrong NJ, Painter KJ, Sherratt JA. A continuum approach to modelling cell–cell adhesion. *J Theor Biol.* 2006;243(1):98-113.
- [48] Murakawa H, Togashi H. Continuous models for cell–cell adhesion. *J Theor Biol.* 2015;374:1-12.
- [49] Carrillo JA, Huang Y, Schmidtchen M. Zoology of a nonlocal cross-diffusion model for two species. *SIAM J Appl Math.* 2018;78(2):1078-104.
- [50] Carrillo JA, Colombi A, Scianna M. Adhesion and volume constraints via nonlocal interactions determine cell organisation and migration profiles. *J Theor Biol.* 2018;445:75-91.
- [51] Gaffney EA, Seirin Lee S. The sensitivity of Turing self-organization to biological feedback delays: 2D models of fish pigmentation. *Math Med Biol.* 2015;32:57-79.
- [52] Konow C, Li Z, Shepherd S, Bullara D, Epstein IR. Influence of survival, promotion, and growth on pattern formation in zebrafish skin. *Sci Rep.* 2021;11(9864).
- [53] Bloomfield JM, Painter KJ, Sherratt JA. How does cellular contact affect differentiation mediated pattern formation? *Bull Math Biol.* 2011;73(7):1529-58.
- [54] Kondo S. An updated kernel-based Turing model for studying the mechanisms of biological pattern formation. *J Theor Biol.* 2017;414:120-7.
- [55] Painter KJ, Bloomfield JM, Sherratt JA, Gerisch A. A nonlocal model for contact attraction and repulsion in heterogeneous cell populations. *Bull Math Biol.* 2015;77(6):1132-65.
- [56] Giacomin G, Lebowitz JL. Phase segregation dynamics in particle systems with long range interactions. I. Macroscopic limits. *J Stat Phys.* 1997;87:37-61.
- [57] Painter KJ, Hillen T. Volume-filling and quorum-sensing in models for chemosensitive movement. *Can Appl Math Quart.* 2002;10(4):501-43.

- [58] Penington CJ, Hughes BD, Landman KA. Building macroscale models from microscale probabilistic models: a general probabilistic approach for nonlinear diffusion and multispecies phenomena. *Physical Review E*. 2011;84(4):041120.
- [59] Hillen T, Painter KJ. Transport and anisotropic diffusion models for movement in oriented habitats. *Lect Notes Math*. 2013;2071:177-222.
- [60] Carrillo JA, Choi YP, Hauray M. The derivation of swarming models: Mean-field limit and Wasserstein distances. In: Muntean A, Toschi F, editors. *Collective Dynamics from Bacteria to Crowds: An Excursion Through Modeling, Analysis and Simulation*. CISM International Centre for Mechanical Sciences. Vienna: Springer Vienna; 2014. p. 1-46.
- [61] Chen Y, Kolokolnikov T. A minimal model of predator–swarm interactions. *J R Soc Interface*. 2014;11:20131208.
- [62] Bruna M, Burger M, Pietschmann JF, Wolfram MT. Active crowds. In: *Active particles, Vol. 3. Model. Simul. Sci. Eng. Technol.*. Birkhäuser/Springer, Cham; 2022. p. 35-73.
- [63] Champagnat N, Ferrière R, Méléard S. Unifying evolutionary dynamics: from individual stochastic processes to macroscopic models. *Theor Popul Biol*. 2006;69(3):297-321.
- [64] Champagnat N, Ferrière R, Méléard S. Individual-based probabilistic models of adaptive evolution and various scaling approximations. *Prog Probab*. 2008;59:75.
- [65] Champagnat N, Ferrière R, Méléard S. From individual stochastic processes to macroscopic models in adaptive evolution. *Stoch Models*. 2008;24:2-44.
- [66] Hansen JP, McDonald IR. *Theory of Simple Liquids*. London: Academic Press; 2006.
- [67] Lushnikov PM, Chen N, Alber M. Macroscopic dynamics of biological cells interacting via chemotaxis and direct contact. *Phys Rev E*. 2008;78:061904.
- [68] Simpson MJ, Landman KA, Hughes BD. Multi-species simple exclusion processes. *Phys A: Stat Mech*. 2009;388:399-406.
- [69] Simpson MJ, Baker RE. Corrected mean-field models for spatially dependent advection-diffusion-reaction phenomena. *Phys Rev E*. 2011;83:51922.
- [70] Markham DC, Simpson MJ, Baker RE. Simplified method for including spatial correlations in mean-field approximations. *Phys Rev E*. 2013;87:62702.
- [71] Wieczorek R. Hydrodynamic limit of a stochastic model of proliferating cells with chemotaxis. *Kinet Relat Models*. 2023;16:373-93.
- [72] Binny RN, Plank MJ, James A. Spatial moment dynamics for collective cell movement incorporating a neighbour-dependent directional bias. *Journal of the Royal Society Interface*. 2015;12(106):20150228.
- [73] Binny RN, James A, Plank MJ. Collective cell behaviour with neighbour-dependent proliferation, death and directional bias. *Bulletin of Mathematical Biology*. 2016;78:2277-301.
- [74] Middleton AM, Fleck C, Grima R. A continuum approximation to an off-lattice individual-cell based model of cell migration and adhesion. *Journal of theoretical biology*. 2014;359:220-32.
- [75] Bruna M, Chapman SJ, Robinson M. Diffusion of particles with short-range interactions. *SIAM Journal on Applied Mathematics*. 2017;77(6):2294-316.

- [76] Johnston ST, Baker RE, Simpson MJ. A new and accurate continuum description of moving fronts. *New Journal of Physics*. 2017;19(3):033010.
- [77] Bruna M, Chapman SJ. Excluded-volume effects in the diffusion of hard spheres. *Physical Review E*. 2012;85(1):011103.
- [78] Patterson LB, Bain EJ, Parichy DM. Pigment cell interactions and differential xanthophore recruitment underlying zebrafish stripe reiteration and *Danio* pattern evolution. *Nat Commun*. 2014;5(5299).
- [79] Walderich B, Singh AP, Mahalwar P, Nüsslein-Volhard C. Homotypic cell competition regulates proliferation and tiling of zebrafish pigment cells during colour pattern formation. *Nat Commun*. 2016;7(1):11462.
- [80] Golse F. The mean-field limit for the dynamics of large particle systems. *Journées Équations aux dérivées Partielles*. 2003.
- [81] Di Francesco M, Fagioli S. Measure solutions for non-local interaction PDEs with two species. *Nonlinearity*. 2013;26(10):2777.
- [82] Takahashi G, Kondo S. Melanophores in the stripes of adult zebrafish do not have the nature to gather, but disperse when they have the space to move. *Pigment Cell Melanoma Res*. 2008;21(6):677-86.
- [83] Parichy DM, Turner JM. Zebrafish *puma* mutant decouples pigment pattern and somatic metamorphosis. *Dev Biol*. 2003;256(2):242-57.
- [84] Chiari G, Delitala ME, Morselli D, Scianna M. A hybrid modeling environment to describe aggregates of cells heterogeneous for genotype and behavior with possible phenotypic transitions. *International Journal of Non-Linear Mechanics*. 2022;144:104063.
- [85] Brunet E, Derrida B. Shift in the velocity of a front due to a cutoff. *Phys Rev E*. 1997;56:2597-604.
- [86] Sontag A, Rogers T, Yates CA. Stochastic drift in discrete waves of nonlocally interacting particles. *Phys Rev E*. 2023;107:014128.
- [87] Bull JA, Byrne HM. The hallmarks of mathematical oncology. *Proc IEEE*. 2022;110(5):523-40.
- [88] Bruna M, Chapman SJ, Robinson M. Diffusion of Particles with Short-Range Interactions. *SIAM J Appl Math*. 2017;77(6):2294-316. Available from: <https://doi.org/10.1137/17M1118543>.
- [89] Franke F, Aland S, Böhme HJ, Voss-Böhme A, Lange S. Is cell segregation like oil and water: asymptotic versus transitory regime. *PLoS Comput Biol*. 2022;18(9):e1010460.
- [90] Nardini JT, Baker RE, Simpson MJ, Flores KB. Learning differential equation models from stochastic agent-based model simulations. *J Roy Soc Interface*. 2021;18:20200987.
- [91] Bull JA, Byrne HM. Quantification of spatial and phenotypic heterogeneity in an agent-based model of tumour-macrophage interactions. *PLOS Comput Biol*. 2023;19(3):e1010994.
- [92] Miyazawa S. Pattern blending enriches the diversity of animal colorations. *Sci Adv*. 2020;6(49).
- [93] McGuirl MR, Volkening A, Sandstede B. Topological data analysis of zebrafish patterns. *Proc Natl Acad Sci USA*. 2020;117(10):5113-24.
- [94] Martinson WD, Schmitchen M, Volkening A, Venkataraman C, Carrillo JA. GitHub repository for “Linking discrete and continuous models of cell birth and migration”. GitHub; 2023. <https://github.com/wdmartinson/Self-Organization-One-Species>.

Supplementary Information for “Linking discrete and continuous models of cell birth and migration”

W. Duncan Martinson¹, Alexandria Volkening², Markus Schmidtchen³, Chandrasekhar Venkataraman⁴, and José A. Carrillo⁵

¹Mathematical Institute, University of Oxford; william.martinson@maths.ox.ac.uk

²Department of Mathematics, Purdue University; avolkening@purdue.edu

³Institute of Scientific Computing, Technische Universität Dresden;
markus.schmidtchen@tu-dresden.de

⁴Department of Mathematics, University of Sussex; c.venkataraman@sussex.ac.uk

⁵Mathematical Institute, University of Oxford; carrillo@maths.ox.ac.uk

April 5, 2024

This supplementary material contains the following:

- §1: additional discussion of our models (including our xanthophore models);
- §2: detailed numerical methods for simulating and relating our discrete and continuous models;
- §3: study of alternative choices in parameter estimation;
- §4: detailed summary of our model initial conditions;
- §5: additional simulations of our models of melanophore dynamics; and
- §6: simulations of our models of xanthophore dynamics.

1 Additional details on our models

Here, we provide additional details on our models of melanophore migration (§1.1) and birth (§1.2), and we introduce our models of xanthophore dynamics (§1.3).

1.1 Background on our models of melanophore migration

Our ABM for cell movement tracks the positions of individual melanophores in time. We use Newton’s second law to model how the coordinates of cell i (namely $\mathbf{M}_i(t)$) change in response to the forces that it experiences from other cells. As in prior models (i.e., [1, 2, 3, 4]), we assume that these forces arise from repulsion between cells as well as drag forces resulting from friction. We take the latter force to be proportional to the velocity of cell i . The differential equation describing the change in cell positions within our domain $\Omega = [-1.5\text{mm}, 1.5\text{mm}]^2$ is thus given by:

$$m_i \frac{d^2 \mathbf{M}_i}{dt^2} = \mathbf{F}_{\text{fric}}^{(i)} + \mathbf{F}_{\text{int}}^{(i)} = -\beta_i \frac{d\mathbf{M}_i}{dt} + \mathbf{F}_{\text{int}}^{(i)}. \quad (\text{S1})$$

where $i \in \{1, 2, \dots, N_M\}$; m_i is the mass of cell i ; $\mathbf{F}_{\text{int}}^{(i)}$ is the net force arising from all cell–cell interactions; and β_i is a parameter controlling the magnitude of the drag forces that each cell experiences. We assume that all cells have the same mass (i.e., $m_i = m$) and coefficient of friction (i.e., $\beta_i = \beta$) in Eqn. (S1). We compute the cell–cell interaction force, $\mathbf{F}_{\text{int}}^{(i)}$, as the sum of all pairwise interactions between cell i and its neighbors. We assume

that each pairwise force is conservative and only depends on the distance between cell i and its neighbor. The function potential, denoted by W_{MM} in Eqn. (3) of the main text, is the same for each cell. Its gradient encodes the repulsive forces that arise from cell–cell interactions.

Since cell mass and acceleration are typically much smaller than frictional and interaction forces, we may consider inertial terms to be negligible without introducing significant errors. This allows us to reduce Eqn. (S1) to the overdamped first-order system:

$$\frac{d\mathbf{M}_i}{dt} \approx \mathbf{F}_{\text{int}}^{(i)} = - \sum_{j=1, j \neq i}^{N_M} \nabla W_{MM}^c(\mathbf{M}_j - \mathbf{M}_i).$$

As we discuss in the main text, the force ∇W_{MM}^c is set to zero if the distance between cells is beyond a threshold distance. We have slightly abused notation by absorbing the friction coefficient, $\beta_i = \beta$, into our potential. Thus, without loss of generality, we may take this parameter value to be equal to unity.

Lastly, we note that a PDE for the spatio-temporal evolution of the melanophore density may be derived using a mean-field argument. In brief, this is done by identifying the set of cell positions, $\{\mathbf{M}_i\}_{i=1}^{N_M}$, with a measure $\mu^{N_M} = N_M^{-1} \sum_{i=1}^{N_M} \delta_{\mathbf{M}_i}$ that places a Dirac-delta distribution at each cell's centre. Using the chain rule, it is readily verified that, for any test function $\phi(x)$,

$$\frac{d}{dt} \int \phi(x) d\mu^{N_M}(x) = \frac{1}{N_M} \sum_{i=1}^{N_M} \nabla \phi(\mathbf{M}_i) \cdot \frac{d\mathbf{M}_i}{dt} = -N_M \int \nabla \phi(x) \cdot \nabla W_{MM}^c(x - y) d\mu^{N_M}(y) d\mu^{N_M}(x).$$

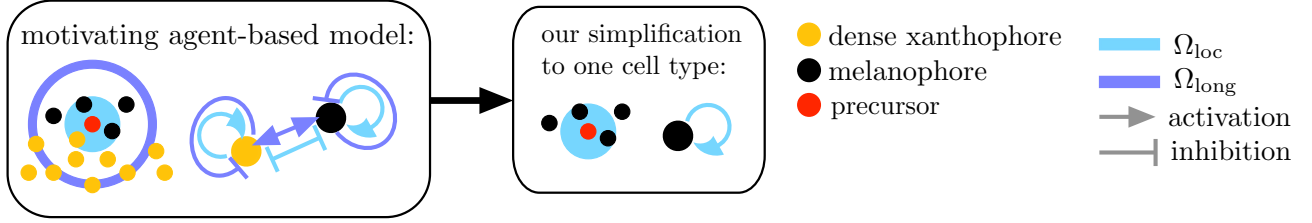
As we are dealing with a large yet finite number of cells, we replace the factor of N_M on the right-hand side by the parameter α_{MM} which we assume to be fixed. Then, the equation becomes

$$\frac{d}{dt} \int \phi(x) d\mu^{N_M}(x) = \frac{1}{N_M} \sum_{i=1}^{N_M} \nabla \phi(\mathbf{M}_i) \cdot \frac{d\mathbf{M}_i}{dt} = -\alpha_{MM} \int \nabla \phi(x) \cdot \nabla W_{MM}^c(x - y) d\mu^{N_M}(y) d\mu^{N_M}(x),$$

Following the procedure in [5, 6], which itself is based on ideas for second-order systems [7, 8], we take the weak limit of the measure μ^{N_M} as the number of particles $N_M \rightarrow \infty$ (again keeping α_{MM} fixed). In this limit, we can link the measure with a probability density, M , that solves the PDE given by Eqn. (4) of the main text. It becomes clear that α_{MM} plays the role of a scaling parameter that accounts for the discrepancy between the mean-field equation corresponding to infinitely many particles and the large system of finitely many particles.

1.2 Background on our ABM rules for melanophore birth

As we discuss in §2.2 of the main text, we base our ABM for cell birth on the prior model [2], which describes cell differentiation. The appearance of new cells is dependent on non-local interactions between melanophores and dense xanthophores. Specifically, motivated by the empirical literature [14, 15, 16, 17, 18, 19], Volkening *et al.* [2] assume that new cells appear at positions selected uniformly at random from across the domain when specific conditions on cell density and proportions are met; see Supplementary Fig. 1. These positions can be thought of as the positions of melanophore precursors or larval xanthophores, widely scattered in the fish skin. In particular, the ABM [2] specifies that a new melanophore appears at the randomly selected position \mathbf{z} when



Supplementary Figure 1: As we discuss in Figure 1 in the main text, our model of cell proliferation is based on the more complex ABM [2]. This model [2] accounts for changes in cell number using stochastic discrete-time rules, which have the overarching form of short-range activation and long-range inhibition [2, 9, 10, 11, 12, 13]. These rules specify that a new melanophore appears at a randomly selected location (red) when there are more melanophores than dense xanthophores locally (in the blue disk) and more dense xanthophores than melanophores at long range (in the purple annulus). (Because precursor cells are not directly taken into account by the model [2], these randomly selected locations are meant to represent the positions of precursors uniformly distributed in the fish skin.) We simplify these rules to make them amenable to the case of a single cell population, reducing the complex birth and death dynamics to short-range activation.

three conditions are met, namely:

$$\underbrace{\sum_{i=1}^{N_M} \mathbb{1}_{\{\mathbf{M}_i \in \Omega_{loc}^z\}}(\mathbf{M}_i) > c_{ABM}^- \sum_{i=1}^{N_X} \mathbb{1}_{\{\mathbf{X}_i \in \Omega_{loc}^z\}}(\mathbf{X}_i)}_{\text{short-range activation: nearby melanophores outnumber xanthophores}} \quad \text{and}$$

$$\underbrace{\sum_{i=1}^{N_X} \mathbb{1}_{\{\mathbf{X}_i \in \Omega_{long}^z\}}(\mathbf{X}_i) > c_{ABM} \sum_{i=1}^{N_M} \mathbb{1}_{\{\mathbf{M}_i \in \Omega_{long}^z\}}(\mathbf{M}_i)}_{\text{long-range inhibition: distant xanthophores outnumber melanophores}} \quad \text{and}$$

$$\underbrace{\sum_{i=1}^{N_M} \mathbb{1}_{\{\mathbf{M}_i \in \Omega_{crowd}^z\}}(\mathbf{M}_i) + \sum_{i=1}^{N_X} \mathbb{1}_{\{\mathbf{X}_i \in \Omega_{crowd}^z\}}(\mathbf{X}_i) < c_{ABM}^+}_{\text{overcrowding prevention: there is enough space to proliferate}} \longrightarrow \text{melanophore appears at } \mathbf{z}, \quad (\text{S2})$$

where

- c_{ABM}^- and c_{ABM} are parameters describing proportions of cells;
- c_{ABM}^+ is an integer-valued number of cells;
- Ω_{loc}^z is a disk centred at \mathbf{z} with radius $75 \mu\text{m}$ capturing interactions between neighboring cells;
- Ω_{crowd}^z is a disk centred at \mathbf{z} with radius $82 \mu\text{m}$ capturing interactions between neighboring cells;
- and Ω_{long}^z is an annulus around \mathbf{z} with inner radius $318 \mu\text{m}$ and width $25 \mu\text{m}$;

see [2]. For our definition of the indicator function, we refer to Eqn. (1) in the main text. As we show in Supplementary Fig. 1, these neighborhoods are based on measurements of cell–cell distances [20] and long cellular extensions [21]. We are interested in the dynamics of one cell population only, so we adjust Eqn. (S2) in three ways to obtain our model:

1. As the long-range inhibition condition guarantees that no melanophores will differentiate without dense xanthophores, we first remove this inequality.

2. To reduce the number of parameters, we next use that $\Omega_{\text{crowd}}^z \approx \Omega_{\text{loc}}^z$ to replace Ω_{crowd}^z with Ω_{loc}^z .
3. Finally, we notice that the right-hand side of the short-range activation inequality in Eqn. (S2) is effectively zero when there are no dense xanthophores present, so we set $c_{\text{ABM}}^- = 0$. Note that, because we have used a weak inequality in the main text, this means that at least one melanophore must be present in the neighborhood Ω_{loc}^z to satisfy this condition.

This leads to our simplified rule for melanophore birth in Eqn. (5) of the main text.

1.3 Models of xanthophore dynamics

While melanophores are separated by about $50 \mu\text{m}$ from one another *in vivo*, xanthophores are roughly $36 \mu\text{m}$ apart [20]. To test that our methods for linking discrete and continuous models can be applied to other cell types that feature different characteristic densities, we thus also develop and simulate models of xanthophore migration and birth. Our models are based on the prior ABM [2] and involve the same corresponding simplifications that we apply for melanophores. In particular, we set:

$$\begin{aligned} \mathbb{R}^2 \ni \mathbf{X}_i(t) &= \text{coordinates of the centre of the } i^{\text{th}} \text{ gold dense xanthophore at time } t, \\ \mathbb{N} \ni N_X(t) &= \text{total number of gold dense xanthophores at time } t, \text{ and} \\ \mathbb{R}_{\geq 0} \ni X(\mathbf{x}, t) &= \text{density of dense xanthophores at position } \mathbf{x} \text{ and time } t \text{ in cells/mm}^2. \end{aligned}$$

Similar to Eqn. (2) for melanophores in the main text, we describe the movement of the i^{th} xanthophore as:

$$\frac{d\mathbf{X}_i}{dt} = - \sum_{j=1, j \neq i}^{N_X} \nabla W_{XX}(\mathbf{X}_i - \mathbf{X}_j), \quad (\text{S3})$$

where $N_X(t) = N_X$ since there is no cell birth, and the cell–cell interaction potential is given by:

$$W_{XX}(\mathbf{r}) = R_{XX} e^{-|\mathbf{r}|/\omega_{XX}}. \quad (\text{S4})$$

Based on [2, 4], we set $R_{XX} = 0.00055 \text{ }^2/\text{day}$ and $\omega_{XX} = 0.011 \text{ mm}$. We do not introduce a cut-off function for the force that xanthophores experience, unlike melanophores, because the values of R_{XX} and ω_{XX} are relatively small. Like our ABM for melanophore birth, our discrete model for xanthophore birth specifies that a new xanthophore appears at the randomly selected location \mathbf{z} according to the rule:

$$\underbrace{\sum_{i=1}^{N_X} \mathbb{1}_{\{\mathbf{X}_i \in \Omega_{\text{loc}}^z\}}(\mathbf{X}_i) \geq 1}_{\text{short-range activation}} \quad \text{and} \quad \underbrace{\sum_{i=1}^{N_X} \mathbb{1}_{\{\mathbf{X}_i \in \Omega_{\text{loc}}^z\}}(\mathbf{X}_i) < \hat{c}_{\text{ABM}}^+}_{\text{overcrowding prevention}} \quad \longrightarrow \quad \text{melanophore appears at } \mathbf{z}, \quad (\text{S5})$$

where $\hat{c}_{\text{ABM}}^+ = 10$ cells and Ω_{loc}^z is given by Eqn. (6) of the main text.

Using the same approach that we apply for melanophores, we find our PDE model of xanthophore migration, as below:

$$\frac{\partial X}{\partial t} = \alpha_{XX} \nabla \cdot (X \nabla W_{XX} \star X), \quad (\text{S6})$$

and our corresponding IDE model of xanthophore birth, namely:

$$\frac{\partial X}{\partial t}(\mathbf{x}, t) = \hat{\gamma} N_{\text{bir}} \mathbb{1}_{\left\{1 < \int_{\Omega_{\text{loc}}^z} X(\mathbf{y}, t) d\mathbf{y} < \hat{c}^+\right\}}(\mathbf{x}, t). \quad (\text{S7})$$

Here W_{XX} is given by Eqn. (S4) with the same parameters as in our ABM results. We fit α_{XX} , $\hat{\gamma}$, and \hat{c}^+ in §6 using the same approach as we apply for melanophores in the main text. (We consider cell migration and birth separately for xanthophores, so we do not present a combined continuous model.)

2 Numerical implementation

To implement Steps 2, 4, and 5 in our pipeline (Fig. 3 of the main text), we generate data by simulating our discrete and continuous models. With one exception in which we consider a 1D domain that is 3 mm long (Fig. 7 of the main text), we implement a 3 mm \times 3 mm domain with periodic boundary conditions in all of our simulations. Following the approach in [2], we measure time in days and simulate all models from $t = 0$ to $t = t_{\text{final}} = 150$ days (unless otherwise noted) with time steps that are model- and cell-behaviour dependent, as we discuss below. We record data from our models at daily intervals (i.e., $t_{\text{record}} = 1$ day) for each simulation.

Implementation of ABM: For our migration-only ABM simulations, we solve Eqn. (2) of the main text using an explicit forward Euler scheme with a time step of $\Delta t_{\text{move}} = 0.01$ days. On the other hand, when we consider the cell birth-only ABM, we implement the stochastic rules in Eqn. (5) of the main text at intervals of $\Delta t_{\text{bir}} = 1$ days. Specifically, at each simulated day, we select N_{bir} sites in the domain, Ω , uniformly at random, simultaneously evaluate them for possible birth, and place a new cell at each position that meets the conditions in Eqn. (5) of the main text. For simulations of our full ABM with melanophore birth and movement, we solve Eqn. (2) of the main text with a time step of $\Delta t_{\text{move}} = 0.1$ days and implement cell birth in time steps of $\Delta t_{\text{bir}} = 1$ day. We apply the same approach to simulate our xanthophore ABM rules in Eqns. (S6) and (S7).

Simulation conditions: The number of ABM realisations we use to compute ensemble average (EA) results depends on the number of cells and ranges from 10^3 to 10^4 . ABM simulations including cell birth use $N_{\text{sim}} = 10^3$ realisations because implementing proliferation becomes computationally expensive as the number of particles increases. To directly compare ABM dynamics with PDE solutions (Step 3 in Fig. 3 of the main text), we sort cell positions from all ABM realisations into a $N_{\text{hist}} \times N_{\text{hist}} \times N_T$ histogram such that each voxel counts the total number of cells within it on a given day. (Because we set $t_{\text{final}} = 2,000$ days for our 1D simulations in Fig. 7 of the main text, we sort cell positions into a histogram every 10 days for this case only.) We then divide by the number of realisations and by the area of each voxel to obtain the EA density in units of cells/mm² (or cells/mm for our 1D simulations). To reduce computational complexity that comes with more cells, we set $N_{\text{hist}} = 30$ voxels in all 2D simulations that include cell birth. For simulations of the migration-only model and 1D simulations of cell birth, we set N_{hist} equal to the number of voxels of the PDE mesh (see below).

Implementation of PDE: We solve our migration-only PDEs, given by Eqn. (4) of the main text and Eqn. (S6), with a first-order finite volume method from [22]. In brief, we discretise Ω by a $N_{\text{bin}} \times N_{\text{bin}}$ mesh with the average density of cells recorded at the centre of each voxel. (We discuss the impact of different choices of N_{bin} in §3 of the main text.) The flux across the boundary of each voxel is approximated by an upwind centred scheme. The time step we use is $\Delta t_{\text{PDE}} = 0.05$ days and data is saved at daily intervals. We solve the IDEs for cell birth—Eqn. (7) of the main text and Eqn. (S7)—using an explicit forward Euler scheme with time step $\Delta t_{\text{bir}} = 1$ day, discretising space uniformly on an $N_{\text{bin}} \times N_{\text{bin}}$ grid. For all of our 2D simulations of cell birth, $N_{\text{bin}} = 64$ voxels; for our 1D simulations in Fig. 7 of the main text, $N_{\text{bin}} = 128$. Lastly, we solve our full PDE model—Eqn. (8) of the main text—on a $N_{\text{bin}} \times N_{\text{bin}}$ mesh in Julia (version 1.7.3) with a time step of $\Delta t_{\text{PDE}} = 0.05$ days and $N_{\text{bin}} = 240$ voxels. We use a first-order explicit scheme to solve Eqn. (8), discretising divergence and flux terms with the aforementioned finite volume scheme and reaction terms with a forward Euler approach. To compare with EA ABM data, we subsequently average voxel values from our continuous models to create a $N_{\text{hist}} \times N_{\text{hist}} \times N_T$ histogram.

Parameter estimation: We estimate the parameters in our models by minimising the squared difference between the histograms associated with our continuous and EA ABM solutions; see Step 4 in Fig. 3 of the main text. To do this, we consider two metrics that account for cell density in space and time and cell mass in time. Our first metric is the squared L^2 difference between the continuous and EA ABM histograms over the

<i>Box</i>		<i>Stripe</i>		<i>Offset rectangles</i>		<i>Two stripes</i>	
N_{bin}	α_{MM}	N_{bin}	α_{MM}	N_{bin}	α_{MM}	N_{bin}	α_{MM}
60	0.4077	60	0.3994	60	0.3806	60	0.3997
120	0.5933	120	0.5817	120	0.5587	120	0.6252
240	0.6420	240	0.6332	240	0.6041	240	0.6387
480	0.6574						

Supplementary Table 1: Optimal values of α_{MM} (unitless) in Eqn. (4) of the main text for our *Box*, *Stripe*, *Offset rectangles*, and *Two stripes* initial conditions and the mesh resolutions defined by N_{bin} . We calculate parameter values according to our procedure in §2 of this SI, based on 10^4 , 10^3 , 10^3 , and 10^3 ABM realisations, respectively.

space-time domain, and we reproduce it from Eqn. (9) in the main text for reference below:

$$\begin{aligned}
e_{L^2}^2 &= \|M_{\text{cts}} - M_{\text{ABM}}\|_{L^2}^2 = \int_{t=0}^{t=t_{\text{final}}} \int_{\Omega} (M_{\text{cts}}(\mathbf{x}, t) - M_{\text{ABM}}(\mathbf{x}, t))^2 d\mathbf{x} dt \\
&\approx \Delta t_{\text{record}} \Delta x \Delta y \sum_{n=0}^{N_T} \sum_{i=1}^{N_{\text{hist}}} \sum_{j=1}^{N_{\text{hist}}} (M_{\text{cts},i,j}^{(n)} - M_{\text{ABM},i,j}^{(n)})^2, \tag{S8}
\end{aligned}$$

where $\Delta t_{\text{record}} = 1$ day; $\Delta x = \Delta y = 3\text{mm}/N_{\text{hist}}$; $M_{\text{cts},i,j}^{(n)}$ is the continuous-model solution at time t_n and position (x_i, y_j) ; and $M_{\text{ABM},i,j}^{(n)}$ is the corresponding EA ABM result. (As an exception, for our 1D simulations in Fig. 7 of the main text, we compute the L^2 difference between the discrete and continuous solutions every 10 days.) For our cell birth-only models we also consider a second metric that minimises the difference in total cell mass produced by our continuous and discrete models. Using the same notation as in Eqn. (S8), we calculate this at time t by:

$$\begin{aligned}
e_{\text{mass}}^2(t) &= \left| \int_{\Omega} M_{\text{cts}}(\mathbf{x}, t) d\mathbf{x} - \int_{\Omega} M_{\text{ABM}}(\mathbf{x}, t) d\mathbf{x} \right|^2 \\
&\approx \left| \left(\Delta x \Delta y \sum_{i=1}^{N_{\text{hist}}} \sum_{j=1}^{N_{\text{hist}}} M_{\text{cts},i,j} \right) - M_{\text{Total,ABM}} \right|^2, \tag{S9}
\end{aligned}$$

where $M_{\text{Total,ABM}}$ denotes the total number of cells in the EA ABM result. We sum this error in mass across all time points, from $t = 0$ to $t = t_{\text{final}}$ with a time step of $t_{\text{record}} = 1$ day in all cases, including our 1D simulations. See Supplementary Fig. 2 for an illustration of how this error in mass depends on γ and c^+ . (Modifying Eqn. (S9) for 1D settings is straightforward, as is modifying Eqns. (S8) and (S9) for xanthophores.) Regardless of whether we consider Eqn. (S8) or (S9), whenever we include cell birth we simulate our discrete models with different N_{bir} and then minimise the summed error according to these equations across N_{bir} values.

To fit our scaling parameters for the cell movement model, α_{MM} and α_{XX} , we minimise Eqn. (S8) since the total cell mass remains constant without birth. We do this using the `least_squares` function from the SciPy library in Python (version 3.9.1) [23], which employs a trust-region reflexive algorithm from [24]. (We use the same approach when we fit the three parameters of the combined model together; see §3 of this SI.) We provide a summary of our estimated values of α_{MM} as a function of mesh resolution and initial condition in Supplementary Table 1; estimates for α_{XX} using the parameter values listed in §6 are given in Supplementary Table 2.

In Supplementary Tables 4 and 5, we present the values of the cell-birth parameters— c^+ , γ , \hat{c}^+ , and $\hat{\gamma}$ —found by minimising Eqn. (S8) or Eqn. (S9), respectively. For both cell types, we observe that the choice

<i>Box</i>		<i>Stripe</i>		<i>Offset rectangles</i>		<i>Two stripes</i>	
N_{bin}	α_{XX}	N_{bin}	α_{XX}	N_{bin}	α_{XX}	N_{bin}	α_{XX}
60	0.1361	60	0.1446	60	0.1383	60	0.1517
120	0.3502	120	0.3789	120	0.3556	120	0.3732
240	0.4766	240	0.5024	240	0.4820	240	0.5015
480	0.5055						

Supplementary Table 2: Optimal values of α_{XX} (unitless) in Eqn. (S6) for the *Box*, *Stripe*, *Offset rectangles*, and *Two stripes* initial conditions as a function of the mesh resolutions defined by N_{bin} . We fit each parameter value according to our procedure in §2 of this SI, based on 5×10^3 , 5×10^3 , 10^3 , and 10^3 ABM realisations, respectively.

Synchronous estimation in 1D			Sequential estimation in 1D		
Error type	c^+ (cells)	γ (mm^{-1})	Error type	c^+ (cells)	γ (mm^{-1})
Cell density	7.430	0.2902	Cell density	7.592	0.2822
Cell mass	7.452	0.2788	Cell mass	7.502	0.2755

Supplementary Table 3: Optimal values of the melanophore density-limiting parameter c^+ and scaling parameter γ in Eqn. (7) of the main text for our 1D simulations; see Fig. 7 of the main text. These results suggest that our estimation procedure is not sensitive to whether we fit c^+ and γ synchronously or sequentially. “Cell density” refers to taking the squared L^2 error in cell density across space and time, and “Cell mass” means we estimate c^+ and γ based on the squared difference between the number of cells predicted by the models in time, without considering spatial effects. We compute the EA ABM result based on 10^3 simulations, and we display numbers in the table to four significant figures.

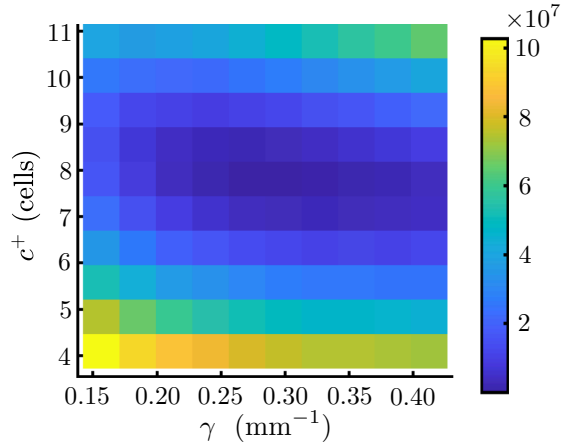
<i>Box</i> for melanophores			<i>Offset rectangles</i> for melanophores		
Error type	c^+ (cells)	γ (mm^{-2})	Error type	c^+ (cells)	γ (mm^{-2})
Cell density	8.564	0.1274	Cell density	8.348	0.1270
Cell mass	8.849	0.1221	Cell mass	8.705	0.1236

Supplementary Table 4: Optimal values of the melanophore density-limiting parameter c^+ and scaling parameter γ in Eqn. (7) of the main text for our 2D simulations; see Fig. 8 of the main text and Supplementary Fig. 8. To check robustness, we fit these parameters separately for two initial conditions (*Box* and *Offset rectangles*) and two measurements of error (namely, the squared L^2 error in the cell density across space and time or the squared L^2 error between the total number of cells—or cell mass—across time); see the caption of Supplementary Table 3. We compute the EA ABM result based on 10^3 simulations, and we round numbers in the table to four significant figures.

of error function does not appear to have a strong effect on the estimates that we obtain. (In particular, the estimates of c^+ and \hat{c}^+ are within at most 7%, and those of γ and $\hat{\gamma}$ are within 4% for each initial condition). Consequently, we opt to minimise Eqn. (S8) for all of the other simulations that we present. Furthermore, in Supplementary Table 3, we present the values of the cell-birth parameters in 1D that we find by fitting both values simultaneously or in a sequential fashion (i.e., first fitting c^+ while keeping γ fixed and then fitting γ

<i>Box</i> for xanthophores		
Error type	\hat{c}^+ (cells)	$\hat{\gamma}$ (mm^{-2})
Cell density	13.45	0.1267
Cell mass	14.43	0.1217

Supplementary Table 5: Optimal values of the xanthophore density-limiting parameter \hat{c}^+ and scaling parameter $\hat{\gamma}$ in Eqn. (S7). For comparison with our melanophore results, we fit these parameters separately for two measurements of error (namely, the squared L^2 error in the cell density across space and time or the squared L^2 error between the total number of cells—cell mass—across time), for the *Box* initial condition; see the caption of Supplementary Table 3. We calculate parameter values according to our procedure in §2 of this SI, first fitting \hat{c}^+ with $\hat{\gamma} = |\Omega|^{-1}$ before finding $\hat{\gamma}$. We simulate 10^3 realisations to produce the EA ABM result and we round numbers in the table to four significant figures. We highlight that $\hat{\gamma}$ for xanthophores and γ for melanophores are very similar, suggesting there is a characteristic timescale of cell birth; see Supplementary Table 4.



Supplementary Figure 2: The squared L^2 difference in total mass between our EA ABM and continuous-model densities as a function of c^+ and γ for the case of cell birth acting alone. We compute this error using Eqn. (S9), integrating over time and summing across all N_{bir} values considered (namely $N_{\text{bir}} = 1, \dots, 10$). We use a time step of $t_{\text{record}} = 1$ day, and our results are based on 10^3 ABM simulations for each N_{bir} value. Compare to Fig. 7 in the main text.

using the optimal value of c^+). We find that both approaches result in nearly identical estimates (Supplementary Table 3). We opt to apply a sequential approach to estimate cell-birth parameters to reduce computational complexity. We perform minimisation for our cell-birth model in MATLAB using the routines `fminbnd` (resp. `fminsearch`) for the sequential (resp. simultaneous) case.

3 Study of alternative choices in parameter estimation

To demonstrate the robustness of our methodology and highlight directions for further improvement, here we present results under some alternative approaches and hyper-parameter values. First, we investigate the effects of the simulation time t_{final} on our parameter estimates; second, we test how the choice of bin resolution when comparing EA ABM and PDE data impacts our results. Lastly, we present our work simultaneously estimating all movement and birth parameters in our combined PDE model.

Study of final simulation time: Because we fit our continuous-model parameters to ABM data in space

and time, the choice of final simulation time, t_{final} may affect our results. To better understand this, we refit the migration scaling parameters (α_{MM} or α_{XX}) in our movement-only model when the final time is $t_{\text{final}} = 50$ days or $t_{\text{final}} = 100$ days, and we compare the resulting parameter values to those from our baseline case when $t_{\text{final}} = 150$ days. For the movement-only model with the *Box* initial condition, fitting to EA ABM data with $t_{\text{final}} = 100$ days yields $\alpha_{\text{MM}} = 0.6479$. (We report parameter values up to four significant figures in this SI text.) Importantly, this is less than a 1% relative difference from the value that we obtain by fitting to EA ABM data with $t_{\text{final}} = 150$ days. Considering EA ABM data with $t_{\text{final}} = 50$ days leads to $\alpha_{\text{MM}} = 0.6465$, which is less than a 1% increase from the value that we find by fitting to data with $t_{\text{final}} = 150$ days. Similarly, fitting with the *Box* initial condition for xanthophores yields $\alpha_{\text{XX}} = 0.4770$ when $t_{\text{final}} = 100$ and $\alpha_{\text{XX}} = 0.4837$ when $t_{\text{final}} = 50$ days. These values of α_{XX} correspond to less than a 1% difference and a 2% difference, respectively, from the values of α_{XX} that we find by fitting to data with $t_{\text{final}} = 150$ days. These observations demonstrate the validity of our parameter estimates over various time horizons.

Study of binning procedure: To test whether the estimated scaling parameters depend on the resolution of the histogram used to bin EA ABM data (N_{hist}), we refit the PDE scaling parameters to ABM data that we binned on a coarser (60×60) mesh. We remark that the PDE itself is solved on a 240×240 mesh and the resulting histogram averaged to obtain a 60×60 mesh that can be directly compared with the EA ABM data. Using this procedure, we find that the values of α_{MM} are 0.6544, 0.6373, 0.6180, and 0.6543 for the *Box*, *Stripe*, *Offset rectangles*, and *Two stripes* initial conditions, respectively. Compared to the α_{MM} values that we obtain from fitting to ABM data on a 240×240 mesh, the relative difference between our estimated parameters based on these different histogram resolutions is approximately 2%, 0.6%, 2%, and 2%, for the *Box*, *Stripe*, *Offset rectangles*, and *Two stripes* initial conditions, respectively. Similarly, for our xanthophore simulations, we find that the relative differences in our estimated values of α_{XX} for a coarser (60×60) binning mesh and our baseline mesh (240×240) are approximately 6%, 5%, 7%, and 7%, for the *Box*, *Stripe*, *Offset rectangles*, and *Two stripes* initial conditions, respectively. (In particular, reporting four significant figures, we find $\alpha_{\text{XX}} = 0.5054$, $\alpha_{\text{XX}} = 0.5263$, $\alpha_{\text{XX}} = 0.5130$, and $\alpha_{\text{XX}} = 0.5342$ for these four initial conditions when we bin ABM data on a coarser mesh.)

Simultaneous estimation of parameter values As we note in the main text, an alternative approach to our modular methodology is to instead identify the values of α_{MM} , γ , and c^+ in our full continuous model at the same time using EA ABM data from the combined (cell birth and movement) discrete model. As an illustrative example, we show the parameter values that we find using this simultaneous estimation procedure for the *Box* and *Offset rectangles* initial conditions with $N_{\text{bir}} = 150$ locations/day in Supplementary Table 6. Importantly, the parameter values from this simultaneous estimation procedure are different than those produced using a modular approach; compare Supplementary Tables 1, 4, and 6. The PDE solutions under the simultaneously estimated parameters produce a lower L^2 error than the solutions generated with parameters from our modular methodology. (In particular, the L^2 error is $3.229 \cdot 10^5$ in our baseline case versus $2.427 \cdot 10^6$ when we estimate parameters simultaneously, for the *Box* initial condition; similarly, the errors are $3.037 \cdot 10^5$ versus $2.236 \cdot 10^6$, respectively, for the *Offset rectangles* initial condition.) We show simulations of our full PDE model with simultaneously estimated parameter values in Supplementary Figures 3–4. The PDE solutions accurately describe the temporal and spatial dynamics of the EA ABM data, as well as the number of cells over time and the radius of the solution support. The speed at which the solution support expands appears to be overestimated by the PDE models, but only slightly.

Comparing Supplementary Figures 3–4 with Figures 10–11 of the main text suggests that the error produced by a simultaneous estimation procedure is lower than the error produced by modular estimation, but the PDE solutions nevertheless qualitatively resemble each other. This suggests that there may be regions of (α_{MM} , γ , c^+)-space for which the errors resulting from both approaches are nearly identical. To investigate this question, we compute the L^2 error between the combined PDE and EA ABM solutions for a range of α_{MM} and γ values, while keeping the value of c^+ fixed to the values in Supplementary Table 6. (As we discuss in the main text, c^+ is uncorrelated with α_{MM} and γ and thus can be considered independent.) The results of this experiment for the *Box* and *Offset rectangles* initial conditions are in Supplementary Figure 5. Both graphs exhibit a “valley”

<i>Box</i>			<i>Offset rectangles</i>		
α_{MM} (unitless)	c^+ (cells)	γ (mm^{-2})	α_{MM} (unitless)	c^+ (cells)	γ (mm^{-2})
1.906	6.628	0.066	1.844	6.632	0.068

Supplementary Table 6: Values of the melanophore continuous-model parameters (α_{MM} , γ , and c^+) that we find by simultaneously optimising the L^2 error between solutions of the full model (Eqn. (8) of the main text) and the EA ABM data for the *Box* and *Offset rectangles* initial conditions. We compare the solutions on a histogram with $N_{\text{hist}} = 30$ voxels in each spatial dimension. We generate EA ABM data using 10^3 realisations with $N_{\text{bir}} = 150$ locations/day. The PDE solution is solved on a mesh with $N_{\text{bin}} = 240$ voxels in each spatial dimension and subsequently averaged to a coarser mesh to compare directly with the EA ABM histogram. We highlight that the parameter estimates for the two initial conditions are very similar, suggesting there is a characteristic timescale of cell birth.

of relatively low error, meaning that parameters that lie within the valley produce roughly similar errors. The parameters that we obtain with a modular and simultaneous estimation procedure lie within (or at least near) this valley, which explains why their respective PDE solution resemble each other. Furthermore, these figures suggest that α_{MM} and γ may not be identifiable when fitting to EA ABM data of the combined model (i.e., it is not possible to find a unique choice of these individual parameters that minimises the L^2 error). This may have connections to the concept of ‘‘sloppiness’’ in biological models, which can play an important role when performing multi-parameter estimation [25], and it suggests directions for future work. Since we will likely not be able to uniquely identify all parameter values from a combined dataset, it makes sense to consider other experiments that can pinpoint these specific values. In this case, by fitting parameters to a movement-only and birth-only model, we are able to find values of α_{MM} , γ , and c^+ that are able to produce PDE solutions that can accurately represent all three scenarios.

4 Detailed initial conditions

For reproducibility, we describe our initial conditions for our melanophore and xanthophore simulations in detail here; see Supplementary Figure 6 for an overview. In both cases, our initial conditions account for empirical observations of cell–cell distances and stripe width [12, 20]. Specifically, the average distance between melanophores is about $50 \mu\text{m}$ in zebrafish patterns, and the average distance between dense xanthophores is roughly $36 \mu\text{m}$ [20]. The average distance between melanophores and xanthophores at stripe–interstripe boundaries, in turn, is about $82 \mu\text{m}$ [20], and (inter)stripes have been estimated to be about 7–12 cells wide [12]. Based on these observations [12, 20], we thus estimate that melanophore and xanthophore densities are about $400 \text{ cells}/\text{mm}^2$ and about $772 \text{ cells}/\text{mm}^2$, respectively.

We base our initial conditions on these values, as below:

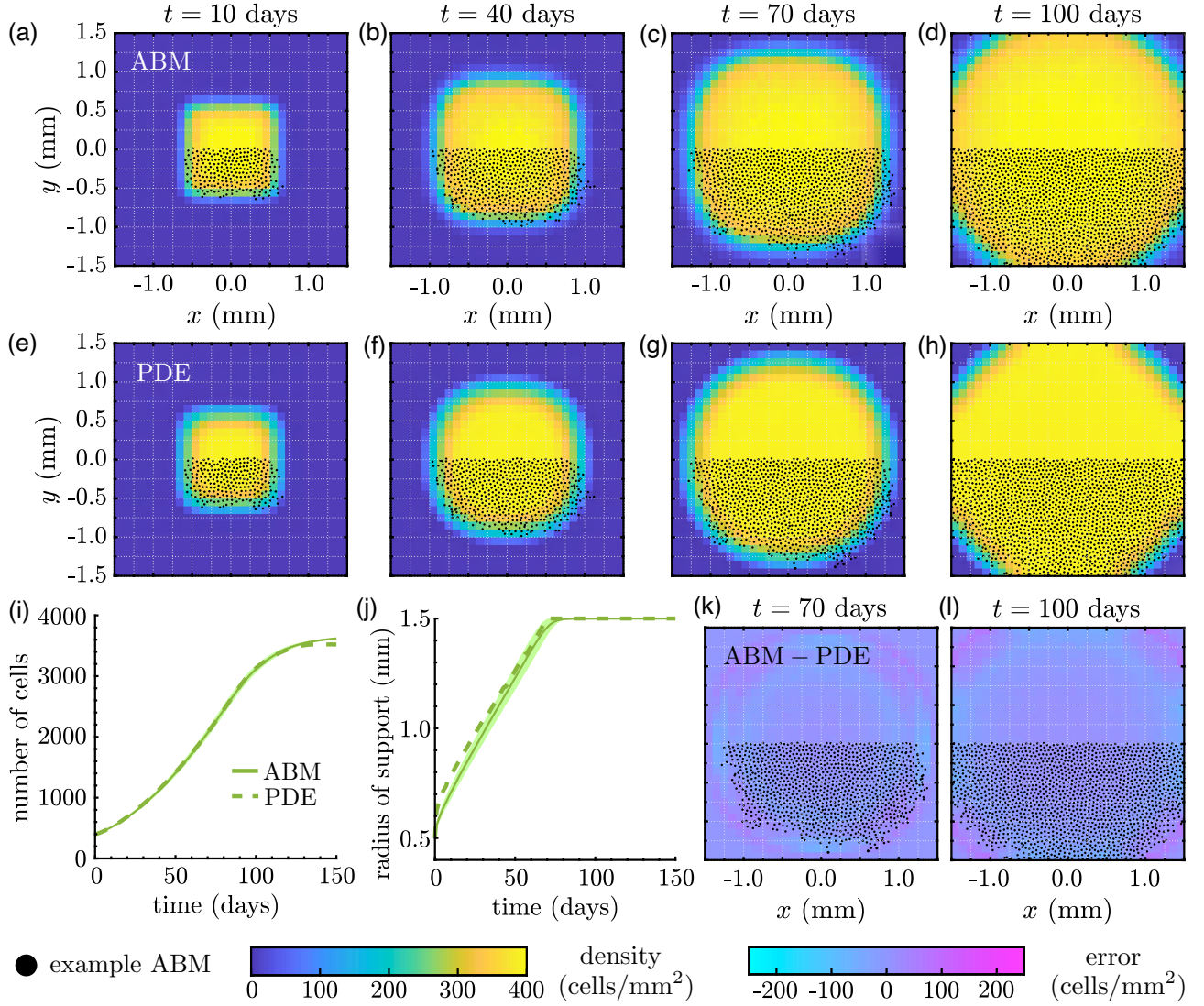
- *Box*: This initial condition (a 1 mm x 1 mm square) is chosen to mimic the symmetry of the domain (a 3 mm x 3 mm square). The PDE and ABM are initialised by:

$$M(x, y, 0) = 400\mathbb{1}_{(x,y) \in [-0.5, 0.5]^2}(x, y), \quad \text{and} \quad \mathbf{M}_i \sim \text{Unif}((x, y) \in [-0.5, 0.5]^2),$$

where $\mathbb{1}_{\text{cond}}(x, y)$ is described by Eqn. (1) of the main text. The xanthophore initial condition is the same but with a density of $772 \text{ cells}/\text{mm}^2$. We sample 400 (resp. 772) cells from this support uniformly at random to create the initial condition for each ABM simulation.

- *Stripe*: This initial condition is motivated by the typical patterning that is observed in wild type zebrafish. The PDE and ABM are initialised by:

$$M(x, y, 0) = 400\mathbb{1}_{x \in [-1.5, 1.5]}(x)\mathbb{1}_{y \in [-0.25, 0.25]}(y)$$



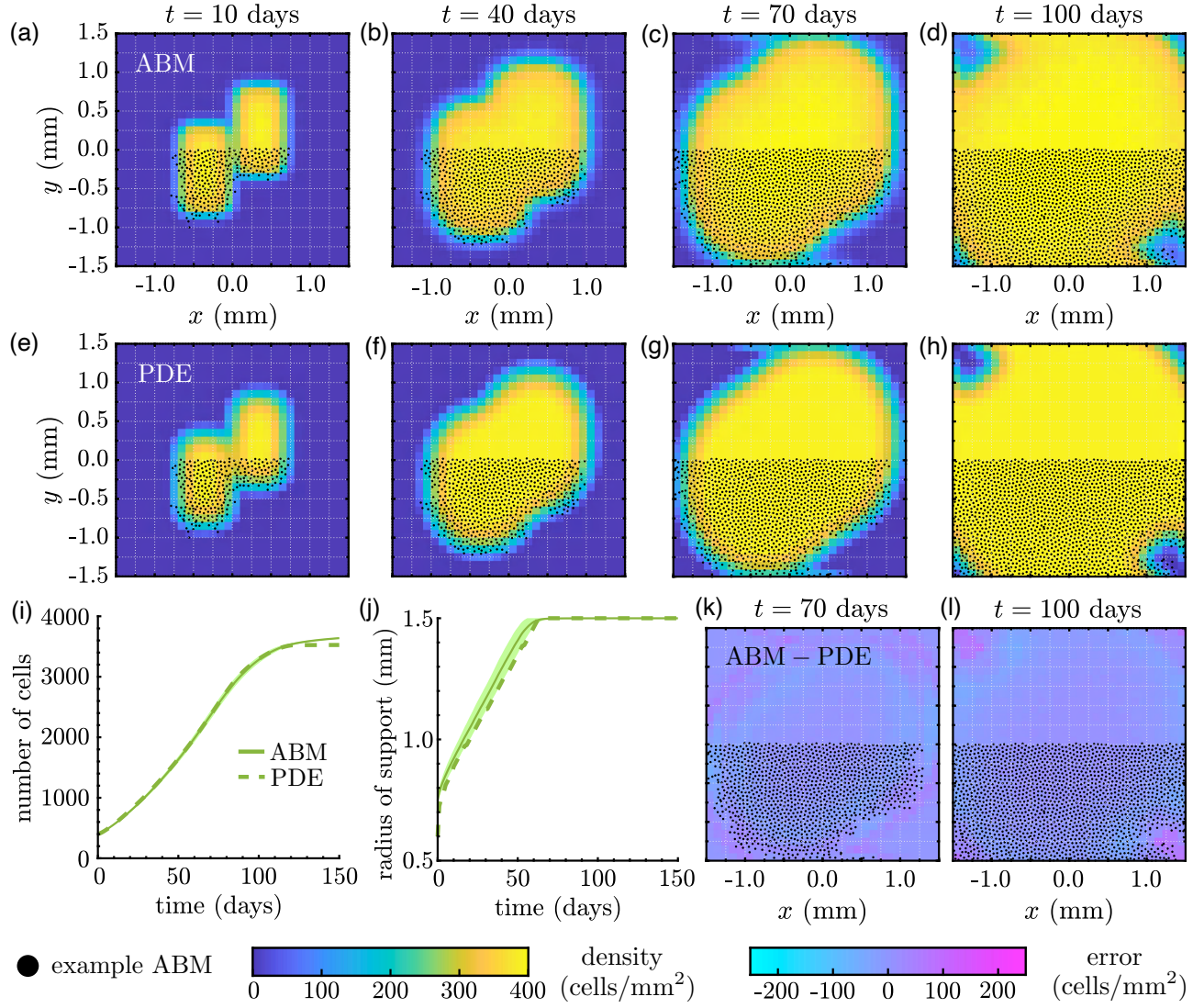
Supplementary Figure 3: Melanophore movement and birth models with our *Box* initial condition, using the parameter values in Supplementary Table 6. We set $N_{\text{bir}} = 150$ positions/day. We show (a)–(d) the EA ABM result (based on 10^3 simulations) and the (e)–(h) PDE solution of Eqn. (8) of the main text. (i) The time evolution of the PDE cell mass and solution support agree well with the ABM data. We compute the radius of support for each ABM realisation and the PDE solution using the approach that we describe in the caption of Figure 10 in the main text. (k)–(l) We show the difference between the PDE and EA ABM solutions from (a)–(h) at two sample times. Cell positions from one ABM simulation are shown to illustrate how the continuous and discrete solutions are related. In (i) and (j), shaded regions denote plus or minus one standard deviation.

as well as

$$\mathbf{M}_i \sim \text{Unif}((x, y) \in [-1.5, 1.5] \times [-0.25, 0.25]).$$

The xanthophore initial condition is the same but with a density of 772 cells/mm². For each ABM simulation, we sample 600 (resp. 1158) cells from this support uniformly at random to create its initial condition.

In addition, we include two more initial conditions which test whether the values of α_{MM} and γ are robust

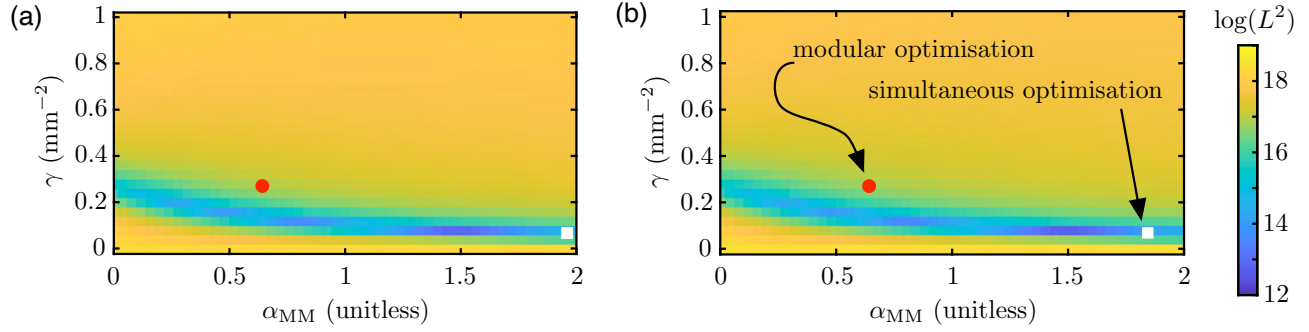


Supplementary Figure 4: Melanophore movement and birth models with our *Offset rectangles* initial condition, using the parameter values in Table 6. Results correspond to the case $N_{\text{bir}} = 150$ positions/day. We show (a)–(d) the EA ABM result (using 10^3 simulations) and (e)–(h) the PDE solution of Eqn. (8) of the main text. (i)–(j) The time evolution of the PDE cell mass and solution support agree well with the ABM data. (k)–(l) We show the difference between the PDE and EA ABM solutions from (a)–(h) at two sample times. We overlay cell positions from one ABM simulation to illustrate how the continuous and discrete solutions are related. In (i) and (j), shaded regions denote plus or minus one standard deviation.

in describing the interactions between disjoint regions of cells, which is not immediately obvious given the nonlocal nature of the model, and whether these values depend on the geometry of the initial condition.

- *Offset rectangles*: This initial condition takes into account non-standard geometries when two disjoint regions meet. We initialise one rectangle for the PDE and ABM simulations as:

$$M(x, y, 0) = 400\mathbb{1}_{x \in [-0.6, -0.1]}(x)\mathbb{1}_{y \in [-0.75, 0.25]}(y),$$



Supplementary Figure 5: Plot of the $\log(L^2)$ error surfaces as a function of α_{MM} and γ for the (a) *Box* and (b) *Offset rectangles* initial conditions, using the respective optimal values of c^+ from Supplementary Table 6. In both cases, we use $N_{\text{bir}} = 150$ positions/day. The red circle marks the values of α_{MM} and γ that we find using a modular estimation procedure (see Supplementary Tables 1 and 4), while the white square corresponds to the values of α_{MM} and γ that we find by optimising all parameters simultaneously (see Supplementary Table 6). The error is calculated by summing the squared difference between the PDE and EA ABM data across space and time, as in Supplementary Eqn. (S8). We note that the parameters found using our simultaneous optimisation procedure do not appear to correspond to the global minimum of the L^2 surface, but to a local minimum.

as well as

$$\mathbf{M}_i \sim \text{Unif}((x, y) \in [-0.6, -0.1] \times [-0.75, 0.25]),$$

while the other rectangle is initialised as:

$$M(x, y, 0) = 400\mathbb{1}_{x \in [0.1, 0.6]}(x)\mathbb{1}_{y \in [-0.25, 0.75]}(y)$$

as well as

$$\mathbf{M}_i \sim \text{Unif}((x, y) \in [0.1, 0.6] \times [-0.25, 0.75]).$$

The xanthophore initial condition is the same but with a density of 772 cells/mm². For each rectangle, we sample 200 (resp. 386) cells uniformly at random from their respective supports to create an ABM simulation's initial condition.

- *Two stripes*: This initial condition is constructed so that two disjoint regions of cells encounter each other; this intends to model the sharp fronts of melanophores (and xanthophores) which are present in living zebrafish. We initialise one stripe for the PDE and ABM simulations as:

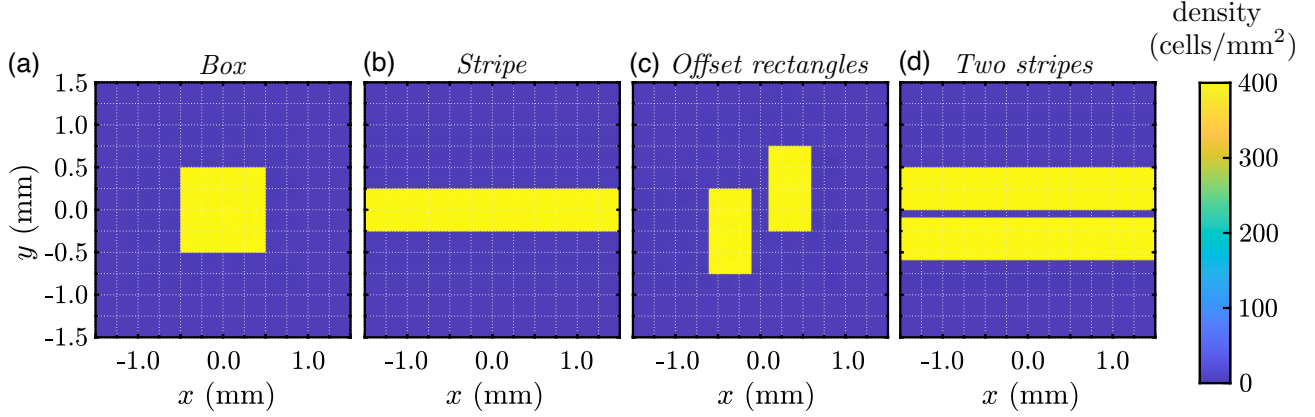
$$M(x, y, 0) = 400\mathbb{1}_{x \in [-1.5, 1.5]}(x)\mathbb{1}_{y \in [0, 0.5]}(y) \quad \text{and} \quad \mathbf{M}_i \sim \text{Unif}((x, y) \in [-1.5, 1.5] \times [0, 0.5]),$$

while the other stripe is initialised as:

$$M(x, y, 0) = 400\mathbb{1}_{x \in [-1.5, 1.5]}(x)\mathbb{1}_{y \in [-0.582, -0.082]}(y),$$

and

$$\mathbf{M}_i \sim \text{Unif}((x, y) \in [-1.5, 1.5] \times [-0.582, -0.082]).$$



Supplementary Figure 6: Summary of the initial conditions for our simulations of melanophore dynamics: (a) *Box*, (b) *Stripe*, (c) *Offset rectangles*, and (d) *Two stripes*.

For each rectangle, we sample 600 cell positions uniformly at random within the respective support to create the ABM initial condition. For xanthophores, the PDE and ABM simulations are initialised as:

$$X(x, y, 0) = 772\mathbb{1}_{x \in [-1.5, 1.5]}(x)\mathbb{1}_{y \in [0, 0.36]}(y), \quad \text{and} \quad \mathbf{X}_i \sim \text{Unif}((x, y) \in [-1.5, 1.5] \times [0, 0.36]),$$

while the other stripe is initialised as:

$$X(x, y, 0) = 772\mathbb{1}_{x \in [-1.5, 1.5]}(x)\mathbb{1}_{y \in [-0.442, -0.082]}(y)$$

as well as

$$\mathbf{X}_i \sim \text{Unif}((x, y) \in [-1.5, 1.5] \times [-0.442, -0.082]).$$

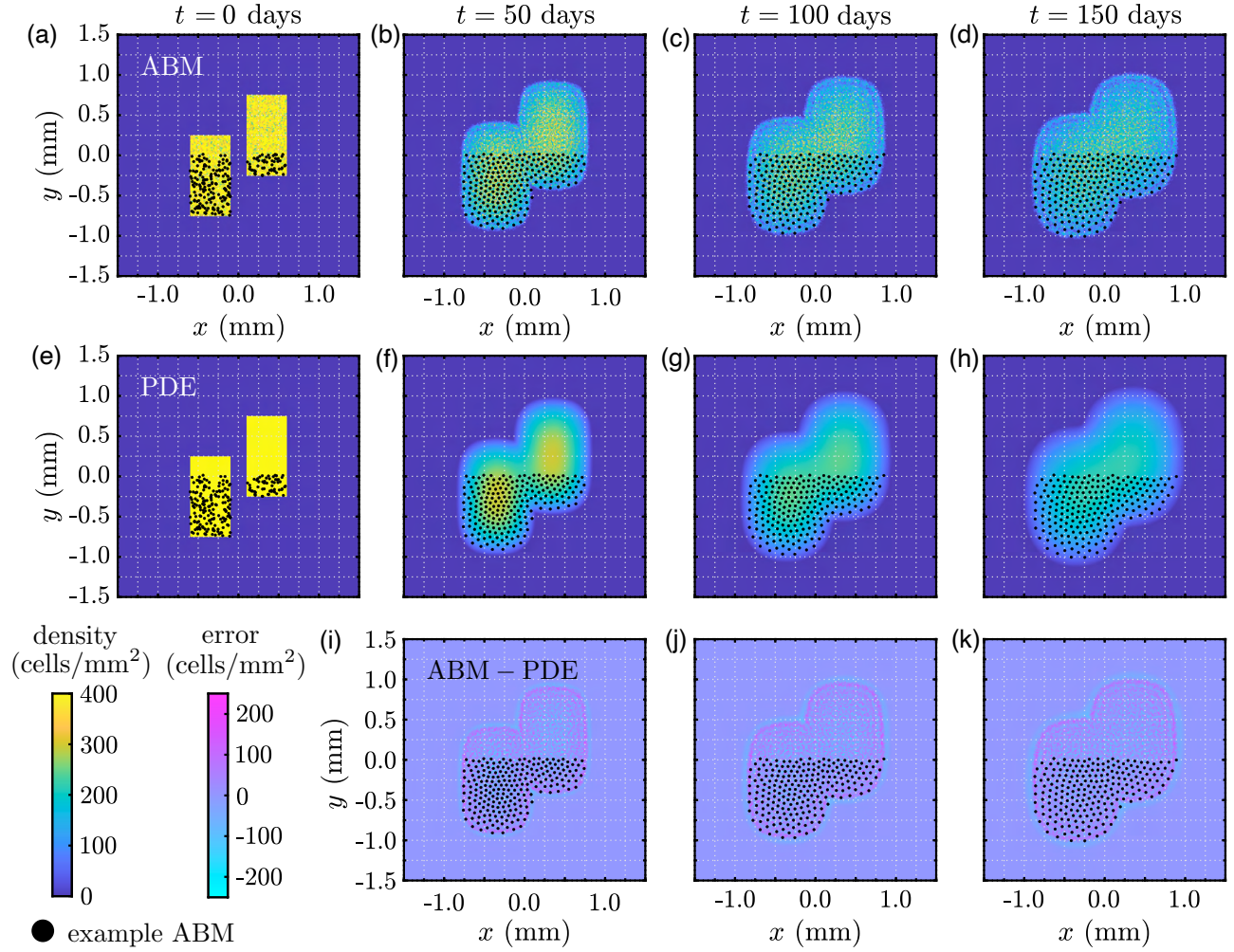
For each rectangle, we sample 1158 xanthophore positions uniformly at random within the respective support to create the ABM initial condition.

5 Additional melanophore simulations

In Supplementary Figures 7 and 8, we present results for our melanophore-movement and melanophore-birth models, respectively, under the *Offset rectangles* initial condition. Similar to our results in §3 of the main text, we find that melanophores spread out from their initial position. Oscillatory bands of high and low cell density emerge near the edge of the EA ABM support for our migration-only simulations in Supplementary Fig. 7. This reflects the small voxel size and relatively short-range strong repulsive forces experienced by individual cells. In comparison to the EA ABM result, we find that our continuous model for melanophore migration accurately captures discrete dynamics within the bulk of the support but otherwise overestimates the result. On the other hand, our continuous model for melanophore birth underestimates the support of the EA ABM result, as we show in Supplementary Fig. 8. Lastly, in Supplementary Figure 9, we highlight the distribution of nearest-neighbor cell–cell distances that arises from our discrete model simulations for melanophores under two example initial conditions.

6 Xanthophore simulations

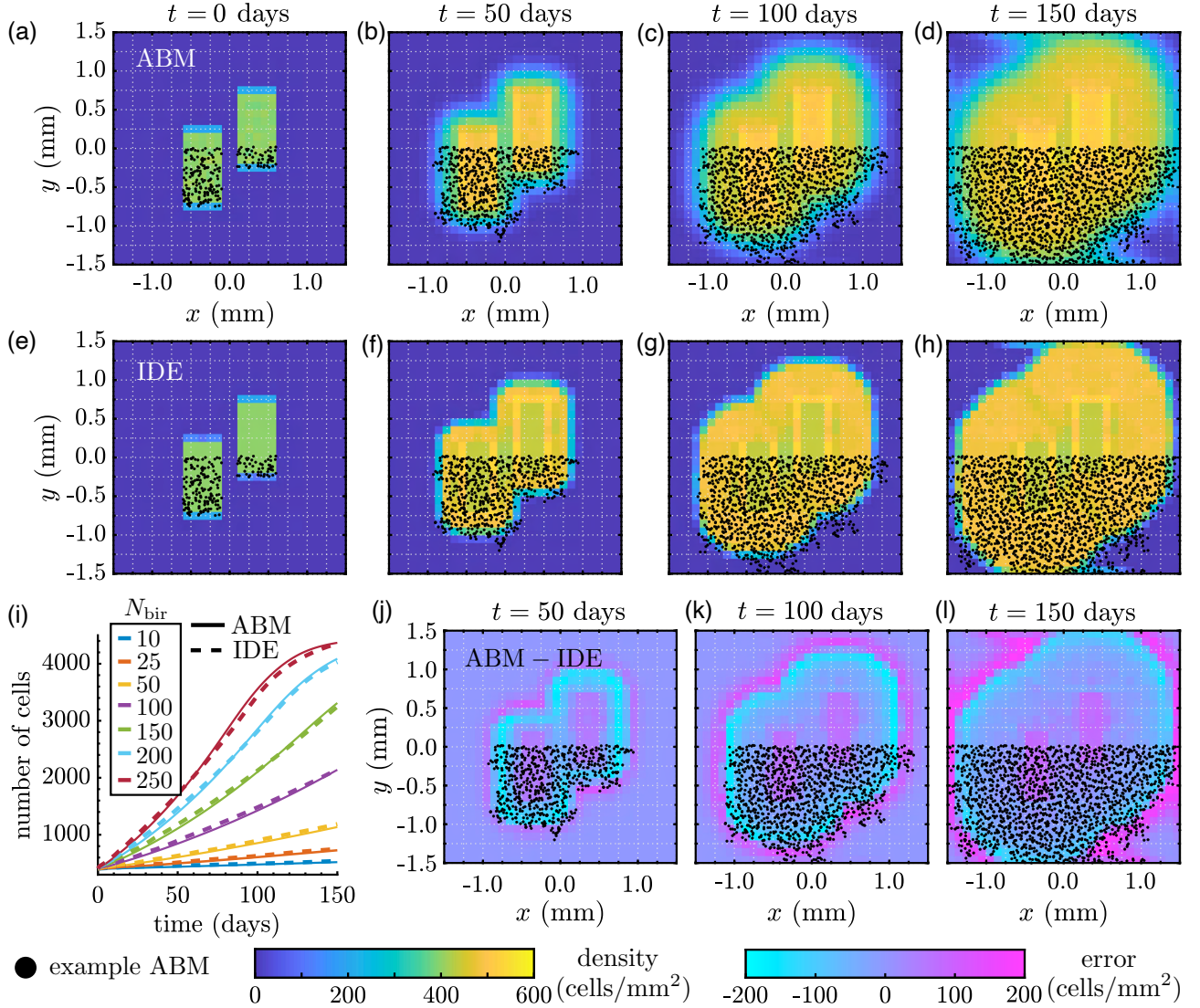
Here we present simulations of our discrete and continuous models of xanthophore behaviour from §1.3, considering movement alone and birth alone, in turn. Our results on xanthophores are similar to our work with



Supplementary Figure 7: Melanophore movement models with our *Offset rectangles* initial condition. We present snapshots of the (a)–(d) EA cell density generated from 10^3 ABM realisations, (e)–(h) PDE results computed using the optimal value of α_{MM} and a mesh resolution of $N_{\text{bin}} = 240$ voxels, and (i)–(k) pointwise difference between the PDE and EA ABM density. We overlay cell positions for one example ABM simulation as a visual guide; we only show about half of the region occupied by these cells. A difference in density of 400 cells/mm² corresponds to about 0.0625 cells per voxel for this choice of mesh resolution. The average pointwise error over the voxels in which at least one of the EA ABM or PDE solutions is non-zero is about 71 cells/mm² at $t = 0$ days, 31 cells/mm² at $t = 50$ days, 30 cells/mm² at $t = 100$ days, and 29 cells/mm² at $t = 150$ days. (These values correspond, respectively, to roughly 18%, 8%, 8%, and 7% of the maximum cell density of 400 cells/mm².)

melanophores, but implementing our pipeline on xanthophores serves two purposes. First, it allows us to test whether our methods are sensitive to cell density and cell–cell distances, as xanthophores are more tightly packed than melanophores [2, 20]. Second, it helps open the door to future studies that may combine the dynamics of melanophores and xanthophores to study pattern formation in more realistic settings. Across our xanthophore results below, we observe similar model behaviour as we did for melanophores. See Supplementary Tables 2 and 5 for the estimated optimal parameter values that we use in simulations of our continuous models.

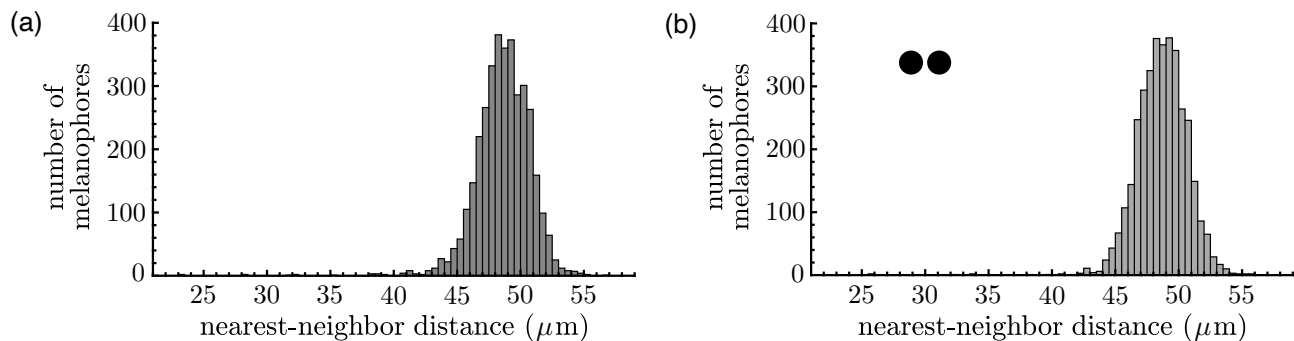
Emulating our approach with melanophore movement, we show the optimal values of α_{XX} in Eqn. S6 as



Supplementary Figure 8: Melanophore birth models with our *Offset rectangles* initial condition. We present (a)–(d) EA ABM results across 10^3 simulations, (e)–(h) the corresponding optimised IDE solution, (i) IDE cell mass in time compared to the mean number of cells across 10^3 ABM simulations for different N_{bir} values, and (j)–(l) the pointwise difference between the IDE and EA ABM results. We overlay cell positions for one example ABM simulation to provide more intuition; we show roughly half of these cells. In (a)–(h) and (j)–(l), we use $N_{\text{bir}} = 150$ positions evaluated for cell birth each day.

a function of different initial conditions and mesh resolutions in Supplementary Fig. 10 and Supplementary Table 2. These results suggest that α_{XX} is independent of the mesh resolution when the latter contains at least 240×240 voxels, corresponding to a mesh spacing of $12.5 \mu\text{m}$. In comparison, empirical observations estimate that xanthophores are about $36 \mu\text{m}$ apart [2, 20]. Moreover, at each mesh resolution in Supplementary Fig. 10(a), the estimated optimal value of α_{XX} does not appear to depend greatly on the initial condition. For example, in the case of a mesh with $N_{\text{bin}} = 240$, the maximum relative difference between the four parameter values is at most 5.5%. Although the errors associated with different initial conditions can vary by an order of magnitude in Supplementary Fig. 10(b), the minimum value of each (roughly convex) curve appears nearly identical.

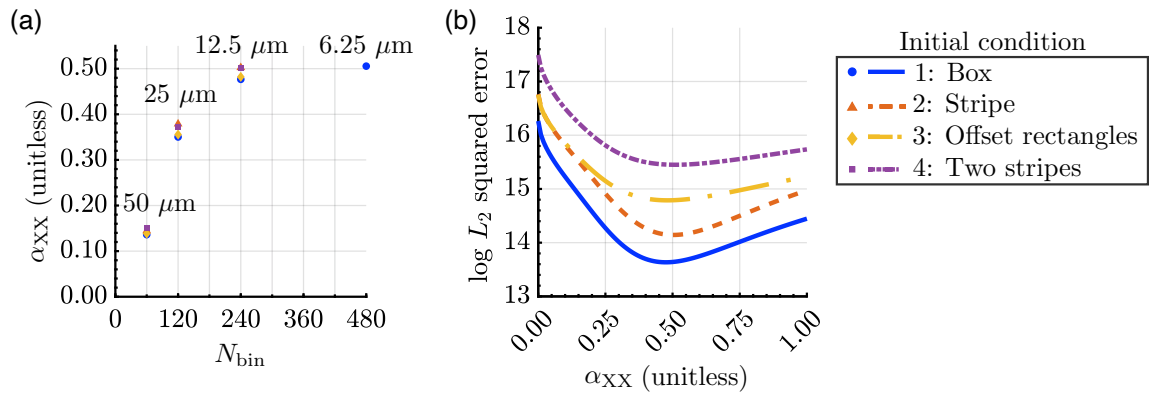
Comparing EA ABM and continuous dynamics, we present results for our xanthophore-movement models



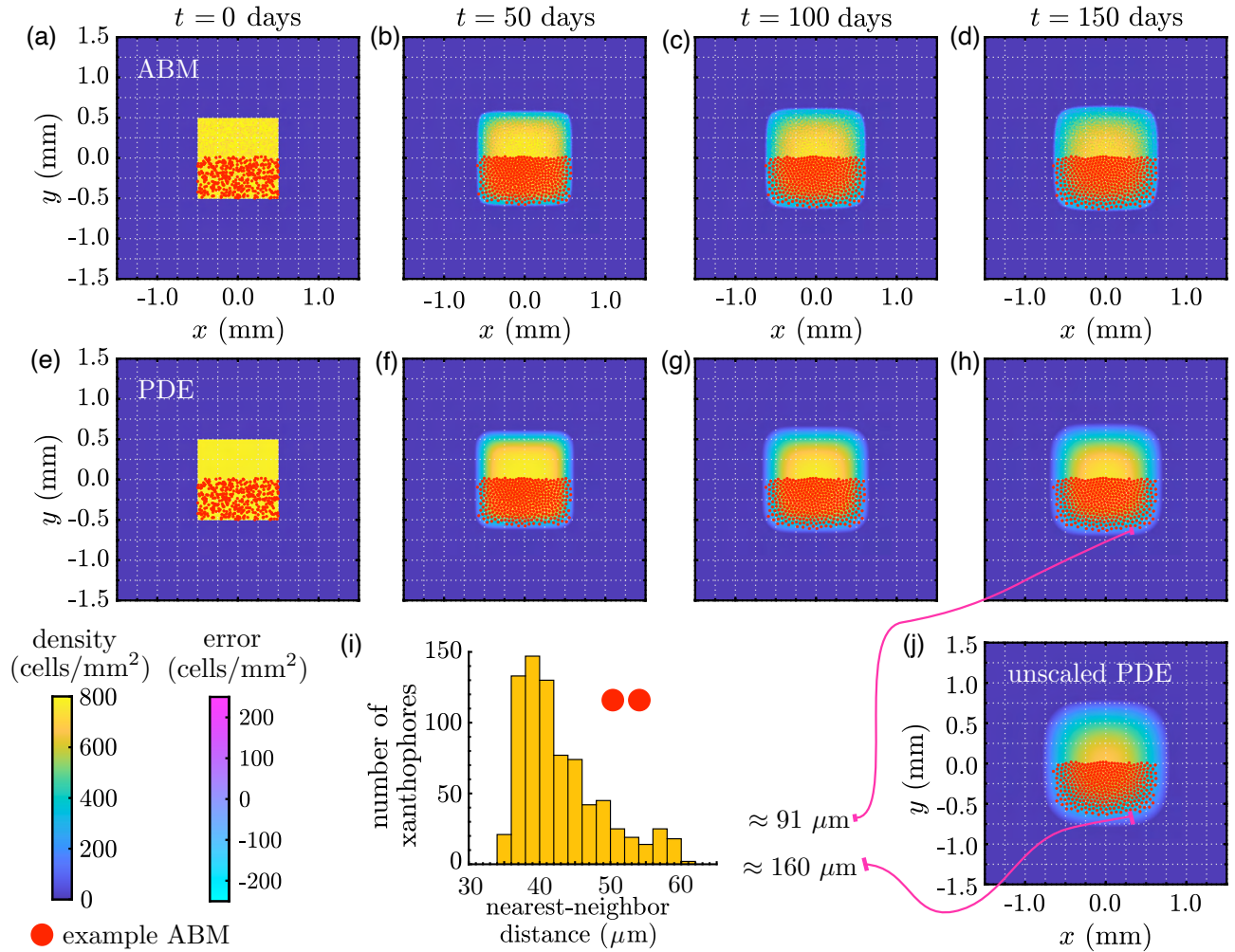
Supplementary Figure 9: Distribution of nearest-neighbor distances for the agent-based model with cell birth and movement. We show the distributions of melanophore–melanophore distances that arise at $t = 150$ days after starting from our (a) *Box* or (b) *Offset rectangles* initial conditions. Each histogram is generated using one realisation of the ABM.

under the *Box*, *Stripe*, *Two stripes*, and *Offset rectangles* initial conditions using our optimal values of α_{XX} and a mesh resolution of $N_{\text{bin}} = 240$ voxels in Supplementary Figures 11–13. (See Eqns. (S3) and (S6).) Notably, we observe an oscillatory band of high and low cell density near the edge of the EA ABM support in Supplementary Fig. 11(a)–(d). This band is almost imperceptible, however, corroborating our argument from the main text that these bands appear due to the interplay between the mesh resolution and the forces that cells experience. Because the forces acting on xanthophores are about an order of magnitude smaller than those for melanophores, we expect to see much fainter bands (if they exist at all).

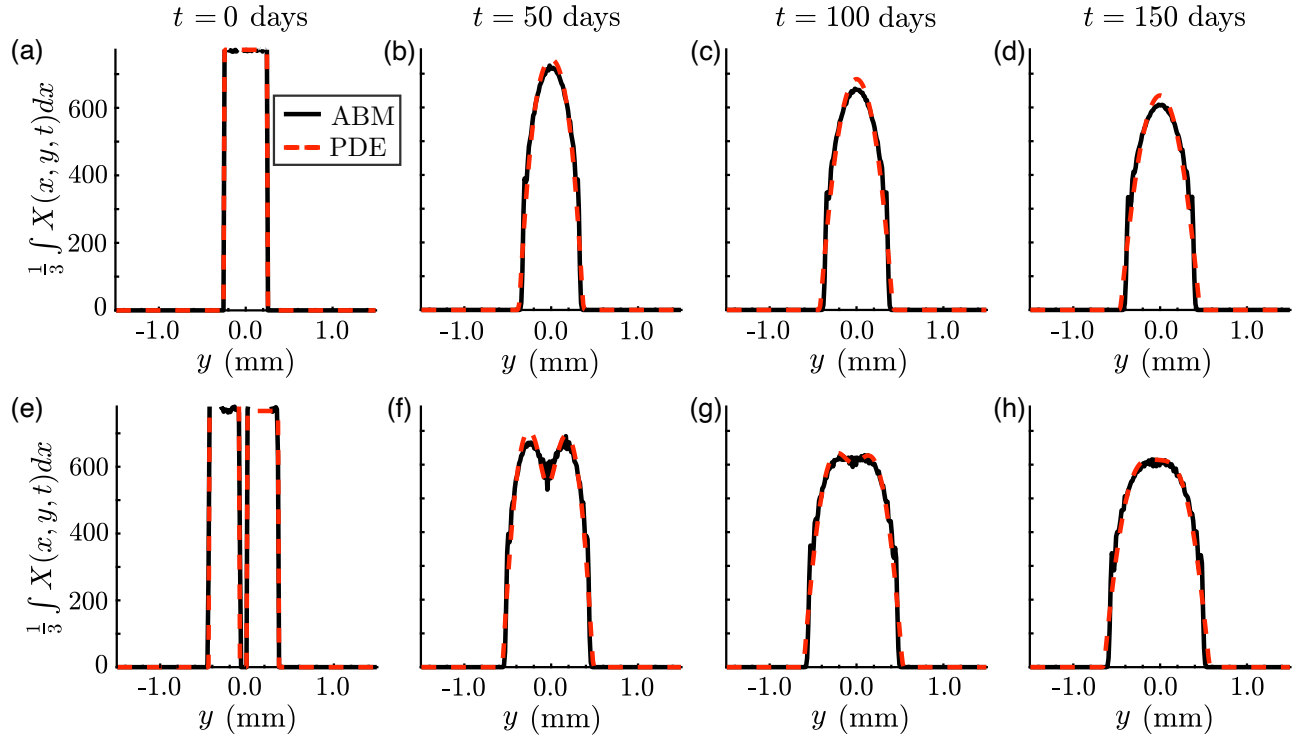
In a corresponding way, we show our results for our xanthophore-birth models—namely Eqns. (S5) and (S7)—given the *Box* initial condition in Supplementary Figures 11. Here we use our optimal values of $\hat{\gamma}$ and \hat{c}^+ based on sequential fitting and minimising the L^2 difference in our IDE and EA ABM histograms in space and time; see Supplementary Table 5. These results are similar to our work with melanophores. We observe that the number of xanthophores is larger in Supplementary Fig. 11(i) compared to Fig. 8 of the main text, a natural consequence of the larger value of the cell-birth limiting parameters \hat{c}_{ABM}^+ and \hat{c}^+ for xanthophores.



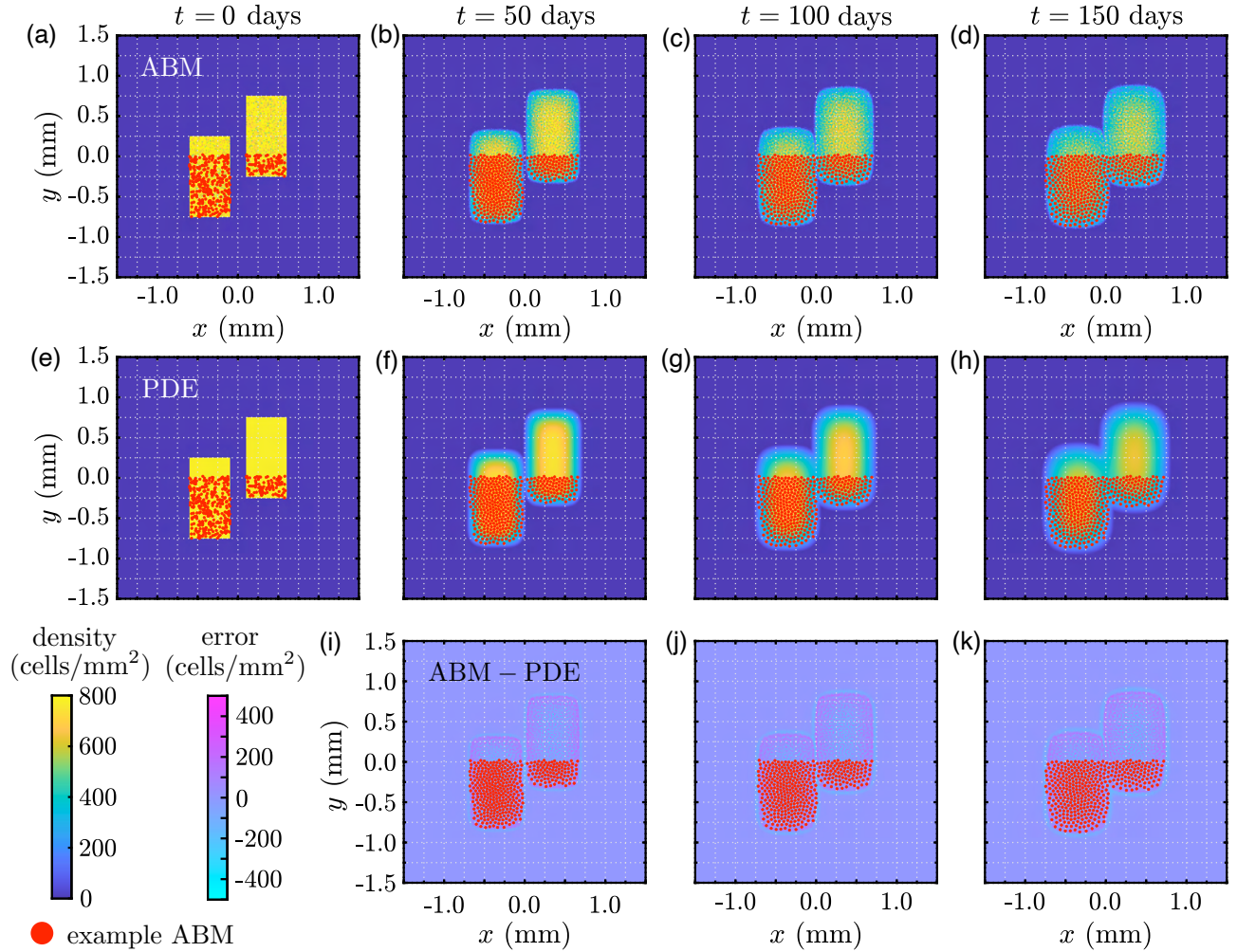
Supplementary Figure 10: The optimal PDE scaling parameter for xanthophore movement depends on the mesh resolution but appears to converge. (a) Scatter plots of the numerically optimised value of α_{XX} from Eqn. (S6) as a function of the mesh resolution, N_{bin} , for all four initial conditions demonstrate that the scaling parameter is correlated with the number of voxels used to simulate our PDE model but appears to converge at sufficiently high ($N_{bin} \geq 240$) mesh resolutions. (b) Plots of the log-squared L^2 error on a $N_{bin} = 240$ mesh, given by Eqn. (S8), as a function of α_{XX} for each initial condition suggest that the values found in (a) are optimal. We refer to §2 of the main text and §2 of this supplementary information for details about numerical computation.



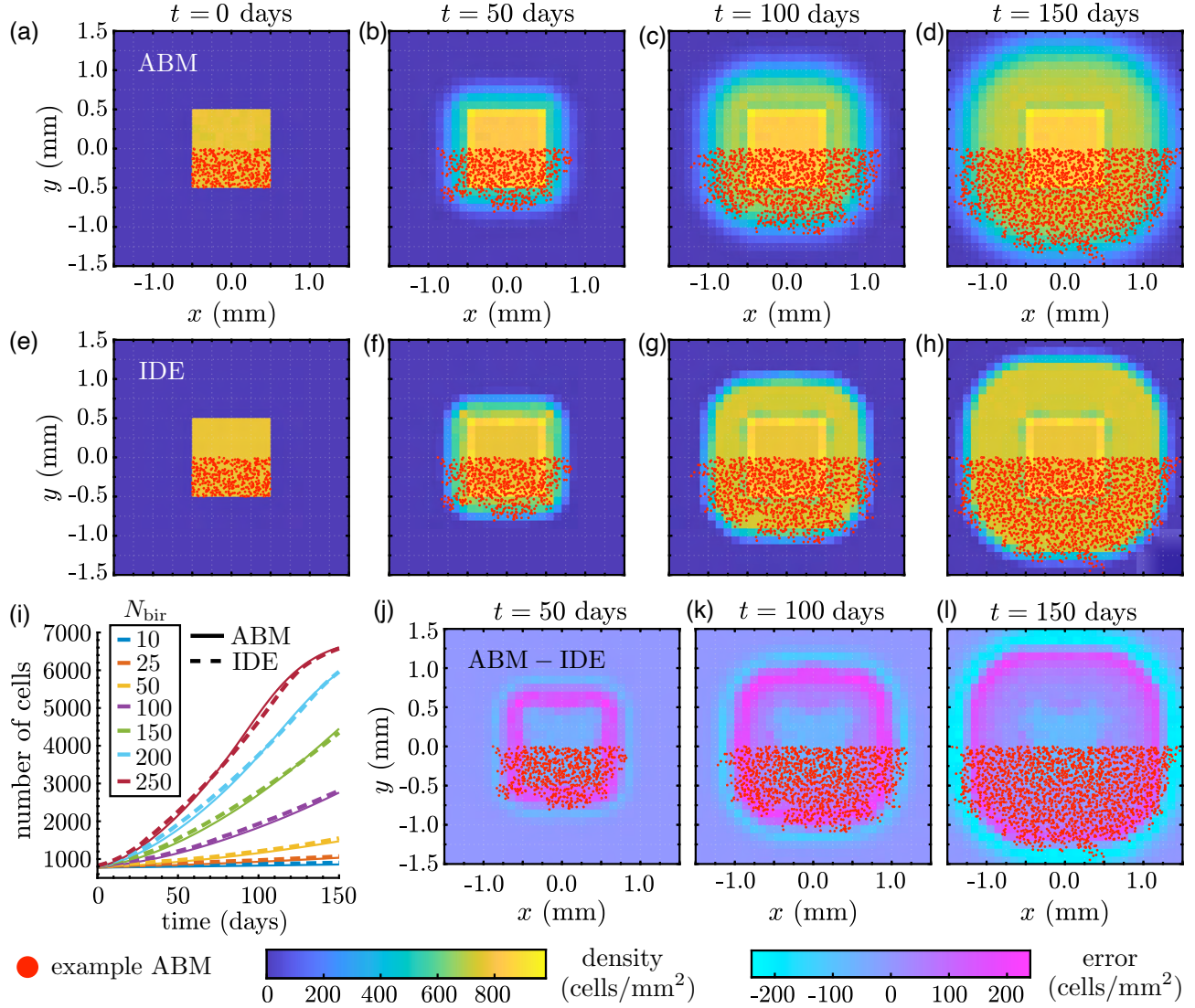
Supplementary Figure 11: Xanthophore movement models with our *Box* initial condition. We present (a)–(d) EA ABM results based on 5×10^3 simulations, (e)–(h) the corresponding PDE solution under the optimal value of α_{XX} for a mesh resolution of $N_{\text{bin}} = 240$ voxels, (i) the distribution of nearest cell–cell distances for an example ABM simulation at 150 days, and (j) the PDE solution with $\alpha_{XX} = 1$ at 150 days for comparison. A difference in cell density of 772 cells/mm^2 corresponds to about 0.12 cells per voxel for this choice of mesh resolution. In (a)–(h) and (j), we overlay cells positions (in red) for an example ABM simulation; we remove the upper region of cells in post-processing for clarity. As we show in (h) and (j), the support of our PDE solution with optimal parameters is about $69 \mu\text{m}$ closer to the ABM support (at the example region shown); this is a difference of about 2 xanthophores based on empirical estimates [20].



Supplementary Figure 12: Xanthophore movement models for our *Stripe* and *Two stripes* initial conditions. (a)–(d) Using a *Stripe* initial condition, we present the column-averaged EA density (cells/mm², black solid line) across 5×10^3 ABM realisations alongside the PDE solution produced with the optimal value of α_{XX} for a mesh with $N_{\text{bin}} = 240$ (dashed red line). We divide by the domain width (3 mm) here to obtain an average density in cells/mm². (e)–(h) Similarly, for a *Two stripes* initial condition, we show the column-averaged EA density (cells/mm², black solid line) over 10^3 ABM realisations alongside the PDE solution under the optimal value of α_{XX} when $N_{\text{bin}} = 240$ (dashed red line). We note that the solutions are nearly uniform in the x -direction (data not shown).



Supplementary Figure 13: Xanthophore movement models with our *Offset rectangles* initial condition. We present (a)–(d) EA ABM results based on 10^3 simulations, (e)–(h) the corresponding PDE solution generated using the optimal value of α_{XX} with a mesh resolution of $N_{\text{bin}} = 240$, and (i)–(k) the pointwise difference between the PDE and EA ABM cell densities. We overlay cell positions from an example ABM simulation in red; we remove the upper region of cells in post-processing.



Supplementary Figure 14: Xanthophore birth models with our *Box* initial condition. We present (a)–(d) EA ABM results based on 10^3 simulations, (e)–(h) the corresponding IDE solution produced with the optimal values of \hat{c}^+ and $\hat{\gamma}$, (i) IDE cell mass compared to the mean number of xanthophores in our EA ABM result in time for different N_{bir} values, and (j)–(l) the pointwise difference between our IDE and EA ABM results. We overlay select cell positions for one representative ABM simulation to provide more intuition. In (a)–(h) and (j)–(l), $N_{\text{bir}} = 150$ positions evaluated for cell birth each day.

References

- [1] D'Orsogna MR, Chuang YL, Bertozzi AL, Chayes LS. Self-propelled particles with soft-core interactions: patterns, stability, and collapse. *Phys Rev Lett*. 2006;96(10):104302.
- [2] Volkening A, Sandstede B. Modelling stripe formation in zebrafish: an agent-based approach. *J R Soc Interface*. 2015;12(112):20150812.
- [3] Carrillo JA, Colombi A, Scianna M. Adhesion and volume constraints via nonlocal interactions determine cell organisation and migration profiles. *J Theor Biol*. 2018;445:75-91.
- [4] Volkening A, Abbott MR, Chandra N, Dubois B, Lim F, Sexton D, Sandstede B. Modeling stripe formation on growing zebrafish tailfins. *Bull Math Biol*. 2020;82(56).
- [5] Bodnar M, Velazquez JLL. Derivation of macroscopic equations for individual cell-based models: a formal approach. *Math Methods Appl Sci*. 2005;28(15):1757-79.
- [6] Di Francesco M, Fagioli S. Measure solutions for non-local interaction PDEs with two species. *Nonlinearity*. 2013;26(10):2777.
- [7] Braun W, Hepp K. The Vlasov dynamics and its fluctuations in the $1/N$ limit of interacting classical particles. *Commun Math Phys*. 1977;56(2):101-13.
- [8] Neunzert H. An introduction to the nonlinear Boltzmann-Vlasov equation. In: Cercignani C, editor. *Kinetic Theories and the Boltzmann Equation*. Lecture Notes in Mathematics. Springer; 1984. p. 60-110.
- [9] Turing AM. The chemical basis of morphogenesis. *Philos Trans R Soc Lond B*. 1952;237(641):37-72.
- [10] Gierer A, Meinhardt H. A theory of biological pattern formation. *Kybernetik*. 1972;12(1):30-9.
- [11] Yamaguchi M, Yoshimoto E, Kondo S. Pattern regulation in the stripe of zebrafish suggests an underlying dynamic and autonomous mechanism. *Proc Natl Acad Sci USA*. 2007;104(12):4790-4793.
- [12] Nakamasu A, Takahashi G, Kanbe A, Kondo S. Interactions between zebrafish pigment cells responsible for the generation of Turing patterns. *Proc Natl Acad Sci USA*. 2009;106(21):8429-34.
- [13] Watanabe M, Kondo S. Is pigment patterning in fish skin determined by the Turing mechanism? *Trends Genet*. 2015;31(2):88-96.
- [14] Budi EH, Patterson LB, Parichy DM. Post-embryonic nerve-associated precursors to adult pigment cells: genetic requirements and dynamics of morphogenesis and differentiation. *PLoS Genet*. 2011;7(5):e1002044.
- [15] Dooley CM, Mongera A, Walderich B, Nüsslein-Volhard C. On the embryonic origin of adult melanophores: the role of ErbB and Kit signalling in establishing melanophore stem cells in zebrafish. *Development*. 2013;140(5):1003-13.
- [16] Singh AP, Nüsslein-Volhard C. Zebrafish stripes as a model for vertebrate colour pattern formation. *Curr Biol*. 2015;25(2):R81-92.
- [17] McMenamin SK, Bain EJ, McCann AE, Patterson LB, Eom DS, Waller ZP, et al. Thyroid hormone-dependent adult pigment cell lineage and pattern in zebrafish. *Science*. 2014;345(6202):1358-61.
- [18] Mahalwar P, Walderich B, Singh AP, Nüsslein-Volhard C. Local reorganization of xanthophores fine-tunes and colors the striped pattern of zebrafish. *Science*. 2014;345(6202):1362-4.

- [19] Parichy D, Spiewak J. Origins of adult pigmentation: diversity in pigment stem cell lineages and implications for pattern evolution. *Pigment Cell Melanoma Res.* 2015;28(1):31-50.
- [20] Takahashi G, Kondo S. Melanophores in the stripes of adult zebrafish do not have the nature to gather, but disperse when they have the space to move. *Pigment Cell Melanoma Res.* 2008;21(6):677-86.
- [21] Hamada H, Watanabe M, Lau HE, Nishida T, Hasegawa T, Parichy DM, Kondo S. Involvement of Delta/Notch signaling in zebrafish adult pigment stripe patterning. *Development.* 2014;141(2):318-24.
- [22] Carrillo JA, Chertock A, Huang Y. A finite-volume method for nonlinear nonlocal equations with a gradient flow structure. *Commun Comput Phys.* 2015;17(1):233-58.
- [23] Virtanen P, Gommers R, Oliphant TE, Haberland M, Reddy T, Cournapeau D, et al. SciPy 1.0: fundamental algorithms for scientific computing in Python. *Nat Methods.* 2020;17(3):261-72.
- [24] Branch MA, Coleman TF, Li Y. A subspace, interior, and conjugate gradient method for large-scale bound-constrained minimization problems. *SIAM J Sci Comput.* 1999;21(1):1-23.
- [25] Gutenkunst RN, Waterfall JJ, Casey FP, Brown KS, Myers CR, Sethna JP. Universally sloppy parameter sensitivities in systems biology models. *PLOS Comput Biol.* 2007 10;3(10):e189.